공학박사학위논문

Accurate and Efficient Computations on Phase-changing Flows in Thermal Vapor Compressor

열압축기 내 다상유동에 대한 정확하고 효율적인 수치해석 연구

2018년 2월

서울대학교 대학원
기계항공공학부
민 대 호

Accurate and Efficient Computations on Phase-changing Flows in Thermal Vapor Compressor

열압축기 내 다상유동에 대한

정확하고 효율적인 수치해석 연구

지도교수 김 종 암

이 논문을 공학박사 학위논문으로 제출함

2017년 12월

서울대학교 대학원

기계항공공학부

민 대 호

민대호의 공학박사 학위논문을 인준함

2017년 12월

위 원 장 김 유 홍 (인)

부위원장 김 종 암 (인)

위 원 이 관 중 (인)

위 원 변 영 환 (인)

위 원 박 원 규 (인)

Abstract

Most previous numerical researches on flow field inside Thermal Vapor Compressor (TVC) has been conducted neglecting phase-changing process around shock-train region. It may provide the plausible results on suction performance of target problem, however, it also can be fallen into erroneous prediction.

The present study focuses above limitations and provides computational improvements through multi-phase flow modeling and analysis. In order to capture the multi-phase flow physics accurately and provide reliable results, several numerical methods and models, including the shock-stable multi-phase AUSMPW+_N scheme, phase-changing models, cell-by-cell adaptive mesh refinement technique, the IAPWS-97 equation of states and its SBTL model, are combined into a numerical solver.

The numerical solver incorporating these methods and models is validated with problems that possess similar physics, phase-changing process, shock-train and its interaction with shear mixing layer. Then fundamental flow physics is introduced, and general operation mode of TVC are reproduced to confirm the consistency of present computations. The influence of grid clustering level on to resolution of shear layer and computed suction performance is shown by examin-

ing grid dependence. Then simulation results on various TVC systems are compared with single- and multi-phase computations. The comparison explain the reason for yielding more accurate results by multi-phase computations than the other. Based on the computational results and comparisons, necessary of describing the phase-changing process and its influence on two major local physical features are addressed. The local flow physics are then compared between multi-phase modelings.

Keywords : Multi-phase computation, Phase-changing model, Thermal Vapor Compressor

Student Number : 2010-30188

Name : Daeho Min

Contents

List of Figures

List of Tables

Chapter 1

Introduction

1.1 Flow fields around TVC

Recently, desalination technology has become prominent as water shortages have become rampant in many countries around the world. It can be categorized into thermal approaches – such as multiple effect distillation and multi-stage flash – and membrane-based approaches – such as sea water reverse osmosis, brackish water reverse osmosis, electro diaysis or reversed electro diaysis. reverse osmotic desalination technology has attracted particular attentions owing to its high efficiency. However, thermal desalination process still remains dom- inant in many geographical regions including Gulf Council countries due to the sea water condition known as 4H: High salinity, High turbidity, High tempera- ture and High marine life.

Thermal vapor compressor (TVC) is a key system for improving

the efficiency of thermal desalination plants. It has two inlets: the primary nozzle to inject steam with high pressure and temperature (called the primary steam), and the suction nozzle to entrain steam with low pressure and temperature (called the suction steam). Figure 1 shows the schematics and application example of a TVC system.

Thermal desalination plant is generally composed of multiple desalination devices as Fig. 2. The saturated steam is injected through the pipe, and sea water is sprayed over it. Then, condensation is occurred in tube by heat exchange, and fresh water can be acquired. At a same time, another steam is generated whose pressure and temperature are lower than of steam in tube via evaporation of sprayed sea water, and this steam is used at next stage unit. The remaining sea water is disposed through the brine line. Because the pressure and temperature of steam are decreased as it passes through multiple devices, desalination efficiency cannot be guaranteed after certain number of unit. At this point, TVC system serves to entrain and repressurize the steam that has low temperature and pressure through the suction nozzle with the highly compressed primary steam. In this sense, the performance of the TVC is generally evaluated in terms of the entrainment ratio (ER), which is defined as the ratio of the mass flow rate between the suction and primary nozzle.

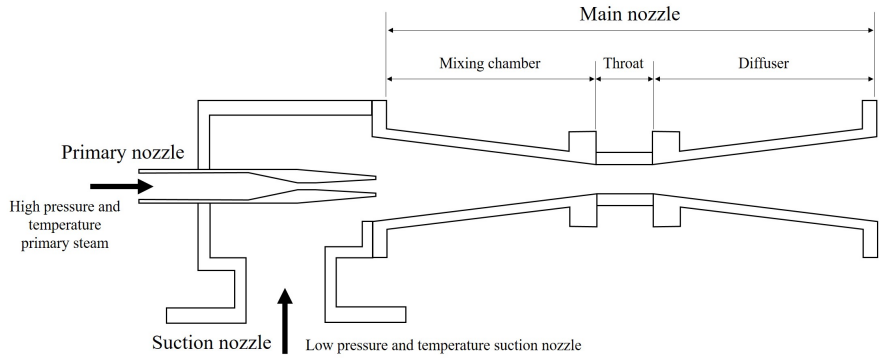

(a) Schematics

(b) Example of application, from Entropie Veolia Corp.

Figure 1: Schematic view and example of application in desalination plant of TVC

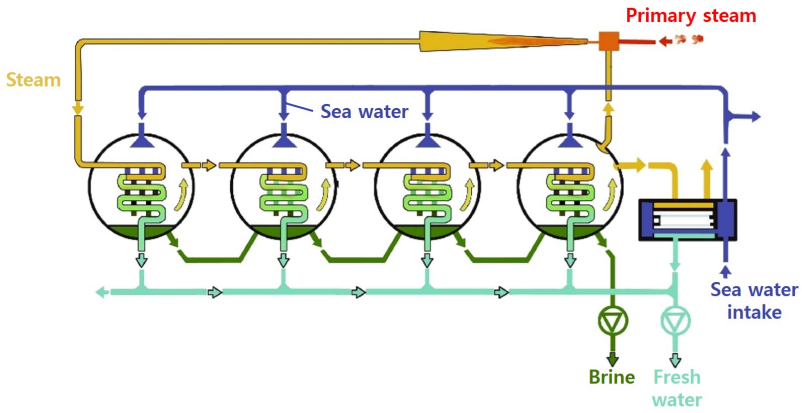

Figure 2: Example of desalination process in plant

Predicting entrainment ratio of TVC is very important in preliminary design state of desalination plant, because it is directly associated with overall efficiency of desalination plant as depicted in Fig. 3 which explains the relation between expectable desalination capacity in each stage and entrainment ratio of TVC. If TVC of high entrainment ratio is adopted in thermal desalination plant, then the amount of overall injection steam in plant is increased, and it hence increases resultant desalination capacity(efficiency) for same amount of primary steam. Therefore, improving the suction performance of TVC is one of top priorities in desalination engineering field, however, complex flow physics associated with entrainment effect makes it difficult to provide reliable and accurate numerical results.

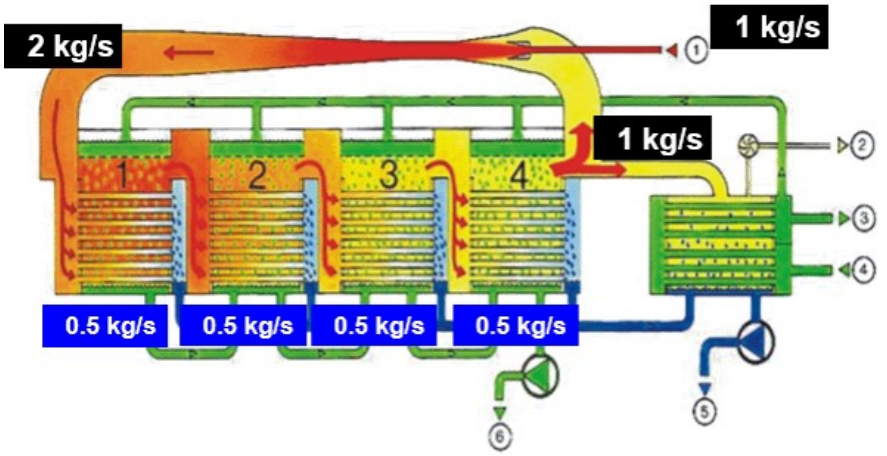

(a) Low efficient TVC, ER = 1

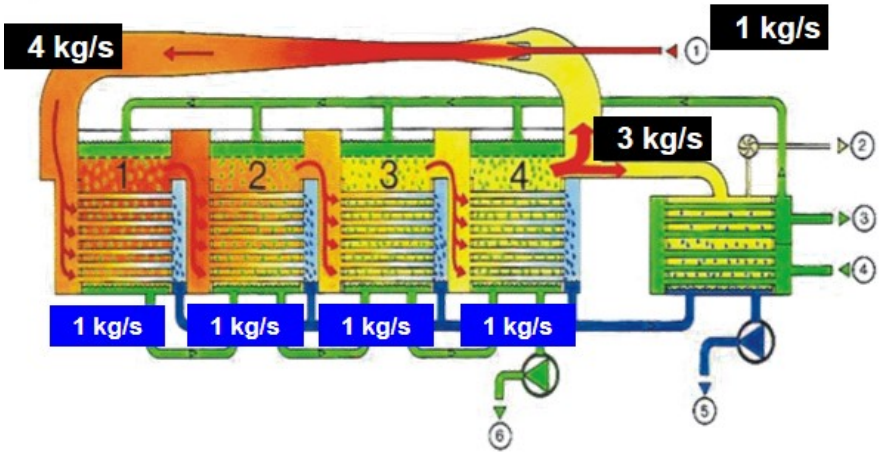

(b) High efficient TVC, ER = 3

Figure 3: Relation between entrainment ratio of TVC and expectable capacity in each desalination unit

The entraining mechanism of TVC arises from momentum transfer between supersonic core flow developed by highly compressed primary stream and stationary surroundings connected to suction stream through a shear layer. At a same time, continuous expansion in the diffusing part of the primary nozzle induces an over-expanded nozzle condition which generates shock at the primary nozzle exit. This shock is reflected as a expansion fan when it reaches to the shear layer, and vice versa. As a result, it develops diamond-shaped shock-train region until supersonic core flow is decelerated into a subsonic flow condition. Unlike a ideal gas flow fields, however, steam flow fields can exhibit phase-changing process due to strong variation of pressure and temperature, and it complicates the entrainment process. Furthermore, interaction between shock-train region and shear layer is a another critical factor for reliable and accurate computations because it determines the structure of the momentum transfer and decaying of supersonic core flow.

Numerous studies have been conducted to understand above physics and to predict suction performance accurately. T. Sriveerakul *et al.* [1] validated their computations with experimental data by comparing the entrainment ratio, and then explained the relations between geometric parameter and flow structure. Wenjian cai *et al.* [2] investi-

gated the relations between two geometric parameters (the primary nozzle exit position and mixing section convergence angle) and suction performance of TVC. Sharifi *et al.* [3] compared the entrainment ratio of five TVC models by changing the converging duct angle. However, all these studies assumed the working fluid as an ideal gas, and hence they neglected the effects on computed suction performance by phase-changing process. They insisted that ideal gas assumption is reasonable choice under the low operating pressure, however, its range of validity were not clearly addressed. Recently, further researches emphasized the necessary of phase-changing models for reliable and accurate computations. It was observed that the predicted entrainment ratio obtained with two-phase computation was greater than that of single-phase computation. This manifested that further investigations are necessary to realize the local flow physics affecting the entrainment ratio.

1.2 Wetness flow and nucleation phenomenon

When pure stream flow is expanded until local pressure drops to saturation value, tiny droplets are continuously generated and disappeared. This fluctuation is leaned toward liquid droplets to be sus-

tained if local pressure drops further. This condensation process is referred as a homogeneous nucleation, which is condensation process without any particles or other droplets.

Historically, there were numerous studies to realize the underlying physics on the homogeneous nucleation such as Volmer *et al.* [4], Zeldovich [5], and McDonald [6, 7]. The classical nucleation theory is established based on their effort to understand fundamental physics on homogeneous nucleation. Furthermore, experimental efforts, measuring the pressure distribution along the centerline of condensing nozzle [8, 9] and droplet size [10, 11], provided reliable data to validate classical nucleation theory. The implementaion of classical nucleation theory on numerical framework and its validation with droplet experimental were given by Young *et al*. He also gave a review of experiments before 1980 and a comparison with his theoretical predictions. The experimental data of Moses *et al.* [10] and Moore *et al.* [11] are used as a validation data in many publications.

On the other hand, there were viewpoint from kinetic theory to realize the phase-changing phenomena. Collier *et al.* [12] and Cammenga [13] estimate the net mass flux of the evaporation and condensation, which is so-called Hertz-Knudsen equation, by assuming an ideal gas and neglecting interactions between individual molecules.

Their definition on net mass flux are modified by introducing the evaporation/condensation coefficient to reflect real gas effects. For the evaporation/condensation coefficients, numerous experimental investigations are carried out by Cammenga [13], Eames *et al.* [14], Bedeaux *et al.* [15] and Marek *et al.* [16]. Because coefficients derived from their study have different order of value, it should be chosen from parametric study based on experimental data.

1.3 Outline of thesis

The present research focuses on accurate and efficient estimation on suction performance of TVC using multi-phase flow computations.

The thesis is organized as follows. The numerical methods and models, which are applied in this research for accurate and efficient computations, are presented in chapter 2. The governing equations to describe the multi-phase flows are firstly introduced. The spatial discretization scheme for robust capturing the compressible flow physics, equation of states to reflect real fluid physics, and other basic numerical methods for turbulent flow are then presented. Two distinct phase-changing modelings to describe the non-equilibrium phase-changing

phenomena, supplementary numerical methods to improve the solution accuracy are followed.

In chapter 3, numerical framework based on approaches introduced in chapter 2 are firstly validated with problems containing similar flow physics. The computations on main object, multi-phase flows inside TVC, is then addressed. The general operation mode of TVC is reproduced to confirm the consistency in computations and explain the major flow physics. The 3-D effect is examined to give the logical validity in computing the target problems with axi-symmetric assumption. The grid dependence on computed solution is then followed. Then, numerical improvement with multi-phase computations and comparison between phase-changing modelings are addressed.

Finally, this thesis will be finished with concluding remarks and discussions on future works.

Chapter 2

Numerical approaches

2.1 Governing equations for multi-phase flows

The present computations are based on the homogeneous mixture model that uses mass fraction to describe two-phase flow fields. In the homogeneous flow theory, the relative motion between each phase is not considered, and a mixture is treated by a set of pseudo-fluid elements whose properties are some averages of each phase component. This is based on the view point that each phase can be properly described by a continuum obtained from a microscopic description using a suitable averaging process. Thus, the governing equation consists of mass-, momentum-, and energy-conservation laws for the mixture, together with a one-phase mass-conservation law. Additionally, the conservation law for the droplet-number density is introduced if a nucleation model is used as a phase-changing model.

Finally, set of above governing equation are cast in integral form for control volume Ω and control surface $\partial\Omega$ as follows:

$$\frac{\partial}{\partial\tau}\int_{\Omega}\mathbf{Q}d\Omega+\oint_{\partial\Omega}\left[(\mathbf{F}_c-\mathbf{F}_v)\cdot\mathbf{n}\right]dS=\int_{\Omega}\mathbf{D}d\Omega \tag{2.1}$$

where $\mathbf{Q}$ is conservative variable vector, $\mathbf{F}_c$ is the inviscid flux tensor, and $\mathbf{F}_v$ is the viscous flux tensor. $\mathbf{D}$ is phase-changing source vector.

$$\mathbf{Q}=\begin{bmatrix}\rho_m & \rho_m u & \rho_m v & \rho_m w & \rho_m E_t & \rho_m Y_1 & \rho_m \eta\end{bmatrix}^T \tag{2.2}$$

$$\mathbf{F}_c=\begin{bmatrix}\rho_m u & \rho_m v & \rho_m w\\ \rho_m u^2+p & \rho_m uv & \rho_m uw\\ \rho_m uv & \rho_m v^2+p & \rho_m vw\\ \rho_m uw & \rho_m vw & \rho_m w^2+p\\ \rho_m uH & \rho_m vH & \rho_m wH\\ \rho_m uY_1 & \rho_m vY_1 & \rho_m wY_1\\ \rho_m u\eta & \rho_m v\eta & \rho_m w\eta\end{bmatrix} \tag{2.3}$$

where ρ_m, p, E_t, H and (u,v,w) represent mixture density, pressure, total energy, total enthalpy and velocity vector, respectively. The mix-

ture density, ρ_m, is calculated using Amagat's law as

$$\frac{1}{\rho_m} = \frac{1-Y_1}{\rho_l} + \frac{Y_1}{\rho_v} \tag{2.4}$$

and the mixture enthalpy is defined as

$$h_m = h_v Y_1 + h_l(1-Y_1) \tag{2.5}$$

Here, subscripts v and l represent vapor and liquid phase, respectively.

The viscous flux tensor $\mathbf{F}_v$ is expressed as

$$\mathbf{F}_v = \begin{bmatrix} 0 & 0 & 0 \\ \tau_{xx} & \tau_{yx} & \tau_{zx} \\ \tau_{xy} & \tau_{yy} & \tau_{zy} \\ \tau_{xz} & \tau_{yz} & \tau_{zz} \\ \theta_x & \theta_y & \theta_z \\ 0 & 0 & 0 \\ 0 & 0 & 0 \end{bmatrix} \tag{2.6}$$

with

$$\begin{aligned}
\theta_x &= u\tau_{xx} + v\tau_{xy} + w\tau_{xz} + q_x \quad , \\
\theta_y &= u\tau_{yx} + v\tau_{yy} + w\tau_{yz} + q_y \quad , \\
\theta_z &= u\tau_{zx} + v\tau_{zy} + w\tau_{zz} + q_z
\end{aligned} \tag{2.7}$$

Here, τ is the viscous tensor, and it can be formulated as follows by assuming Newtonian fluid

$$\tau_{ij} = \mu\left(\frac{\partial u_i}{\partial x_j} + \frac{\partial u_j}{\partial x_i} - \frac{2}{3}\frac{\partial u_k}{\partial x_k}\delta_{ij}\right) \tag{2.8}$$

where μ is molecular viscosity coefficient. The molecular viscosity μ in the viscous stress tensor (2.8) is evaluated by summing a mixture laminar and a turbulent viscosity based on the *eddy viscosity hypothesis* of Boussinesq.

$$\mu = \mu_L + \mu_T \tag{2.9}$$

The heat flux, q in Eqn. (2.7), is computed by Fourier's law,

$$q_i = -k\frac{\partial T}{\partial x_i} \tag{2.10}$$

where k is the thermal conductivity coefficient.

Above governing equations are then converted from the conservative form to a primitive form because the equation of state adopted

in this study, IAPWS-97 or its SBTL model, computes the thermodynamics properties as a function of pressure and temperature. Therefore, the governing equation is summarized as follows:

$$\Gamma \frac{\partial}{\partial \tau} \int_{\Omega} \mathbf{Q_p} d\Omega + \oint_{\partial\Omega} \left[(\mathbf{F}_c - \mathbf{F}_v) \cdot \mathbf{n} \right] dS = \int_{\Omega} \mathbf{D} d\Omega \tag{2.11}$$

$$\mathbf{Q_p} = \begin{bmatrix} p & u & v & w & T & Y_1 & \eta \end{bmatrix}^T \tag{2.12}$$

$$\Gamma = \frac{\partial Q}{\partial Q_p} = \begin{bmatrix} \frac{\partial \rho_m}{\partial p} & 0 & 0 & 0 & \frac{\partial \rho_m}{\partial T} & \frac{\partial \rho_m}{\partial Y_1} & 0 \\ u\frac{\partial \rho_m}{\partial p} & \rho_m & 0 & 0 & \frac{\partial \rho_m}{\partial T}u & \frac{\partial \rho_m}{\partial Y_1}u & 0 \\ v\frac{\partial \rho_m}{\partial p} & 0 & \rho_m & 0 & \frac{\partial \rho_m}{\partial T}v & \frac{\partial \rho_m}{\partial Y_1}v & 0 \\ w\frac{\partial \rho_m}{\partial p} & 0 & 0 & \rho_m & \frac{\partial \rho_m}{\partial T}w & \frac{\partial \rho_m}{\partial Y_1}w & 0 \\ H^* & \rho_m u & \rho_m v & \rho_m w & H\frac{\partial \rho_m}{\partial T} + \rho\frac{\partial h}{\partial T} & \rho_m \frac{\partial h_m}{\partial Y_1} + H\frac{\partial \rho_m}{\partial Y_1} & 0 \\ Y_1\frac{\partial \rho_m}{\partial p} & 0 & 0 & 0 & Y_1\frac{\partial \rho_m}{\partial T} & \rho_m + Y_1\frac{\partial \rho_m}{\partial Y_1} & 0 \\ \eta\frac{\partial \rho_m}{\partial p} & 0 & 0 & 0 & \eta\frac{\partial \rho_m}{\partial T} & \eta\frac{\partial \rho_m}{\partial Y_1} & \rho_m \end{bmatrix} \tag{2.13}$$

where

$$H^* = H\frac{\partial \rho_m}{\partial p} + \rho_m \frac{\partial h}{\partial p} - 1 \tag{2.14}$$

2.2 Spatial discretization scheme

A robust and accurate shock-capturing scheme is a key ingredient in this study because the flow fields in the TVC system contains the shock-train and its interaction with the shear layer. Adopting a

Roe-type scheme, for example, often leads to failed computations due to the shock instability and positivity problem [17]. Hence, a AUSM-type scheme is preferred to cope with the problems associated with strong compressible waves. The AUSMPW+ scheme was originally developed to elliminate the numerical oscillations of the AUSM+ scheme near wall or across strong shocks [18]. However, employing the original AUSMPW+ scheme for multi-phase flow computations turned out to be invalid because the drastic density difference in the gas and liquid phases could yield erroneous numerical dissipation [19]. Based on previous observations, newly developed multi-phase AUSMPW+ scheme (called AUSMPW+_N scheme) [20] for general EOS at all-speeds will be used as a baseline scheme in this study.

The numerical flux at a cell-interface of the AUSMPW+_N scheme is given by

$$E_{1/2} = \bar{M}_L^+ c_{1/2} Q_L + \bar{M}_R^- c_{1/2} Q_R + \bar{P}_L^+ P_L + \bar{P}_R^- P_R. \tag{2.15}$$

In Eq. (2.15), subscripts L and R indicate interpolated values at the left and right state with respect to the cell-interface, respectively. Subscript $1/2$ indicates the value at the cell-interface. The speed of sound

at the cell-interface, $c_{1/2}$, is evaluated from the density-weighted averages of the left and right values.

One of the main features of the AUSMPW+_N scheme is to control the amount of the numerical dissipation by the pressure-based weighting functions ω and $f'_{L,R}$ as follows:

For $M_{1/2} \geq 0$,

$$\begin{cases} \bar{M}_L^+ = & M_L^+ + \\ & M_R^- \left[(1-\omega)\left(1+f_R^{'}\right) - f_L^{'} \right], \\ \bar{M}_R^- = & M_R^- \omega \left(1+f_R^{'}\right). \end{cases} \tag{2.16}$$

For $M_{1/2} < 0$,

$$\begin{cases} \bar{M}_L^+ = & M_L^+ \omega \left(1+f_L^{'}\right), \\ \bar{M}_R^- = & M_R^- + \\ & M_L^+ \left[(1-\omega)\left(1+f_L^{'}\right) - f_R^{'} \right]. \end{cases} \tag{2.17}$$

In Eqs. (2.16) and (2.17), $M_{1/2} = M_L^+ + M_R^-$, and $M^{\pm}$ is the Mach

number splitting function defined by

$$M^{\pm} = \begin{cases} \pm 0.25\,(M \pm 1)^2 & \text{if } |M| \leq 1, \\ 0.5\,(M \pm |M|) & \text{otherwise.} \end{cases} \tag{2.18}$$

The pressure-based weighted function ω is then defined as

$$\omega = \max(\omega_1, \omega_2) \tag{2.19}$$

with

$$\omega_1 = 1 - \Pi_{1/2}^{**^3},$$

$$\omega_2 = 1 - \left(\frac{\min\left(\bar{P}^*_{1,L}, \bar{P}^*_{1,R}, \bar{P}^*_{2,L}, \bar{P}^*_{2,R}\right)}{\max\left(\bar{P}^*_{1,L}, \bar{P}^*_{1,R}, \bar{P}^*_{2,L}, \bar{P}^*_{2,R}\right)} \right)^2. \tag{2.20}$$

Similarly, $f'_{L,R}$ is given by

$$f'_{L,R} = \left(\frac{\bar{P}^*_{L,R}}{\bar{P}^*_s} - 1 \right) \times (1 - \omega_2) \tag{2.21}$$

with $P^*_s = P^+_L P_L + P^-_R P_R + 0.5\rho_{1/2} {c_{1/2}}^2$.

The shock-discontinuity-sensing term (SDST) of Eq. (2.20), $\Pi^{**}_{1/2}$, which plays a crucial role in determining the amount of the numerical dissipation in the AUSMPW+_N scheme, is computed using the

leveled local pressure $\bar{P}^*_{L,R}$ as

$$\Pi^{**}_{1/2} = \min\left(\frac{\bar{P}^*_L}{\bar{P}^*_R}, \frac{\bar{P}^*_R}{\bar{P}^*_L}\right) \tag{2.22}$$

with $\bar{P}^*_{L,R} = P_{L,R} + \min(\rho_L, \rho_R)\, c^2_{1/2,m}$. Thus, $\Pi^{**}_{1/2}$ can be obtained regardless of the type of EOS.

The pressure splitting function $P^{\pm}$ is defined as

$$P^{\pm} = \begin{cases} 0.25\,(M \pm 1)^2\,(2 \mp M) \quad \text{if} \quad |M| \le 1, \\ \pm\alpha M\left(M^2 - 1\right)^2 \\ 0.5\,(1 \pm sign\,(M)) \quad \text{otherwise} \end{cases} \tag{2.23}$$

with $\alpha = 3/16$.

2.3 Compact scheme for viscous flux

The viscous flux in Eq. (2.1) is computed by using second order central differencing. The followings are possible nine components for

three-dimensional case:

$$\begin{array}{ccccc}
\frac{\partial}{\partial\xi}\left(\alpha\frac{\partial q}{\partial\xi}\right) & , & \frac{\partial}{\partial\xi}\left(\alpha\frac{\partial q}{\partial\eta}\right) & , & \frac{\partial}{\partial\xi}\left(\alpha\frac{\partial q}{\partial\zeta}\right) \\
\frac{\partial}{\partial\eta}\left(\alpha\frac{\partial q}{\partial\xi}\right) & , & \frac{\partial}{\partial\eta}\left(\alpha\frac{\partial q}{\partial\eta}\right) & , & \frac{\partial}{\partial\eta}\left(\alpha\frac{\partial q}{\partial\zeta}\right) \\
\frac{\partial}{\partial\zeta}\left(\alpha\frac{\partial q}{\partial\xi}\right) & , & \frac{\partial}{\partial\zeta}\left(\alpha\frac{\partial q}{\partial\eta}\right) & , & \frac{\partial}{\partial\zeta}\left(\alpha\frac{\partial q}{\partial\zeta}\right)
\end{array} \tag{2.24}$$

In Eq. (2.24), α contains the molecular and turbulent viscosity, the Jacobian, and the metrics of the transformation. The q denotes the primitive variable.

The non-cross derivative components, for example, are discretized by using compact three-point formula as follows:

$$\begin{aligned}
\frac{\partial}{\partial\xi}\left(\alpha\frac{\partial q}{\partial\xi}\right) = & \frac{\alpha_{i+1,j,k}+\alpha_{i,j,k}}{2}\left(q_{i+1,j,k}-q_{i,j,k}\right) \\
& -\frac{\alpha_{i,j,k}+\alpha_{i-1,j,k}}{2}\left(q_{i,j,k}-q_{i-1,j,k}\right)
\end{aligned} \tag{2.25}$$

The cross derivative components are discretized by using the fol-

lowing nine-point formula:

$$\frac{\partial}{\partial\xi}\left(\alpha\frac{\partial q}{\partial\eta}\right) = \frac{\alpha_{i+1,j,k}+\alpha_{i,j,k}}{8}\left[\left(q_{i+1,j+1,k}-q_{i,j+1,k}\right)\right.$$
$$\left.-\left(q_{i+1,j-1,k}-q_{i,j-1,k}\right)\right]$$
$$-\frac{\alpha_{i,j,k}+\alpha_{i-1,j,k}}{8}\left[\left(q_{i,j+1,k}-q_{i-,j+1,k}\right)\right.$$
$$\left.-\left(q_{i,j-1,k}-q_{i-1,j-1,k}\right)\right] \qquad (2.26)$$

2.4 Time integration method

In this chapter, LU-SGS time integration method, which is firstly introduced by Yoon *et al*. [21], is presented. It uses lower-upper factorization and Gauss-Seidel relaxation on governing equation, Eq.(2.11). The governing equation in differential form is

$$\frac{\Gamma}{J}\frac{\partial Q_p}{\partial\tau}+\frac{\partial E}{\partial\xi}+\frac{\partial F}{\partial\eta}+\frac{\partial G}{\partial\zeta}=\frac{\partial E_v}{\partial\xi}+\frac{\partial F_v}{\partial\eta}+\frac{\partial G_v}{\partial\zeta}+D \qquad (2.27)$$

To form the matrix equation, pseudo-time derivative term is expressed with 1st-order euler discretization as

$$\frac{\Gamma}{J}\frac{\partial Q_p}{\partial\tau}\approx\frac{\Gamma\triangle Q_p}{J\triangle\tau} \qquad (2.28)$$

while convective flux derivative terms are discretized with Taylor ex-

pansion

$$\frac{\partial}{\partial \xi}\left(E^{n+1}\right) \approx \frac{\partial}{\partial \xi}\left(E+\frac{\partial E}{\partial Q_p}\right]^n \triangle Q_p\Bigg) = \frac{\partial E}{\partial \xi}^n + \partial_\xi A_p \triangle Q_p \quad (2.29)$$

$$\frac{\partial}{\partial \eta}\left(F^{n+1}\right) \approx \frac{\partial}{\partial \eta}\left(F+\frac{\partial F}{\partial Q_p}\right]^n \triangle Q_p\Bigg) = \frac{\partial F}{\partial \eta}^n + \partial_\eta B_p \triangle Q_p \quad (2.30)$$

$$\frac{\partial}{\partial \zeta}\left(G^{n+1}\right) \approx \frac{\partial}{\partial \zeta}\left(G+\frac{\partial G}{\partial Q_p}\right]^n \triangle Q_p\Bigg) = \frac{\partial G}{\partial \zeta}^n + \partial_\eta C_p \triangle Q_p \quad (2.31)$$

The viscous flux derivative terms are expressed as

$$\frac{\partial}{\partial \xi}\left(E_v^{n+1}\right) \approx \frac{\partial}{\partial \xi}\left(E_v+\frac{\partial E_v}{\partial Q_p}\right]^n \triangle Q_p\Bigg) = \frac{\partial E_v}{\partial \xi}^n + \partial_\xi A_{v,p} \triangle Q_p \quad (2.32)$$

$$\frac{\partial}{\partial \eta}\left(F_v^{n+1}\right) \approx \frac{\partial}{\partial \eta}\left(F_v+\frac{\partial F_v}{\partial Q_p}\right]^n \triangle Q_p\Bigg) = \frac{\partial F_v}{\partial \eta}^n + \partial_\eta B_{v,p} \triangle Q_p \quad (2.33)$$

$$\frac{\partial}{\partial \zeta}\left(G_v^{n+1}\right) \approx \frac{\partial}{\partial \zeta}\left(G_v+\frac{\partial G_v}{\partial Q_p}\right]^n \triangle Q_p\Bigg) = \frac{\partial G_v}{\partial \zeta}^n + \partial_\eta C_{v,p} \triangle Q_p \quad (2.34)$$

Based on Eq. (2.28)$\sim$(2.34), governing equation is re-expressed as

$$\begin{aligned}
&\frac{\Gamma\triangle Q_p}{J\triangle\tau}+\partial_\xi A_p\triangle Q_p+\partial_\eta B_p\triangle Q_p+\partial_\zeta C_p\triangle Q_p \\
&\quad-\partial_\xi A_{v,p}\triangle Q_p-\partial_\eta B_{v,p}\triangle Q_p-\partial_\zeta C_{v,p}\triangle Q_p \\
&\quad=-\frac{\partial E^n}{\partial\xi}-\frac{\partial F^n}{\partial\eta}-\frac{\partial G^n}{\partial\zeta}+\frac{\partial {E_v}^n}{\partial\xi}+\frac{\partial {F_v}^n}{\partial\eta}+\frac{\partial {G_v}^n}{\partial\zeta}+D \quad (2.35)
\end{aligned}$$

In following equations, right hand side terms in Eq. (2.35) will be summarized as RHS. The equation (2.35) is simplified as

$$\left[\frac{I}{J\triangle\tau}+\partial_\xi\tilde{A}_p+\partial_\eta\tilde{B}_p+\partial_\zeta\tilde{C}_p-\partial_\xi\tilde{A}_{v,p}-\partial_\eta\tilde{B}_{v,p}-\partial_\zeta\tilde{C}_{v,p}\right]\triangle Q_p=\Gamma^{-1}RHS \tag{2.36}$$

where

$$\tilde{A}_p=\Gamma^{-1}A_p$$

$$=\begin{bmatrix}
\frac{\rho_m\frac{\partial h_m}{\partial T}\frac{1}{c^2}U}{SS} & \frac{\xi_x\frac{\partial h_m}{\partial T}\rho_m^2}{SS} & \frac{\xi_y\frac{\partial h_m}{\partial T}\rho_m^2}{SS} & \frac{\xi_z\frac{\partial h_m}{\partial T}\rho_m^2}{SS} & 0 & 0 & 0 \\
\frac{\xi_x}{\rho_m} & U & 0 & 0 & 0 & 0 & 0 \\
\frac{\xi_y}{\rho_m} & 0 & U & 0 & 0 & 0 & 0 \\
\frac{\xi_z}{\rho_m} & 0 & 0 & U & 0 & 0 & 0 \\
0 & \frac{\xi_x\rho_m\left(1-\frac{\partial h_m}{\partial p}\rho_m\right)}{SS} & \frac{\xi_y\rho_m\left(1-\frac{\partial h_m}{\partial p}\rho_m\right)}{SS} & \frac{\xi_z\rho_m\left(1-\frac{\partial h_m}{\partial p}\rho_m\right)}{SS} & U & 0 & 0 \\
0 & 0 & 0 & 0 & 0 & U & 0 \\
0 & 0 & 0 & 0 & 0 & 0 & U
\end{bmatrix} \tag{2.37}$$

In Eq. (2.37), $SS = \rho_m \frac{\partial h_m}{\partial T} \frac{1}{c^2}$.

By applying lower-upper factorization, Eq .(2.36) yields

$$LD^{-1}U\triangle Q_p = \Gamma^{-1}RHS \tag{2.38}$$

where

$$\begin{aligned}
L = \Bigg[& \frac{1}{J\triangle\tau} + \alpha\left(|\lambda_{\tilde{A}}|_{max} + |\lambda_{\tilde{B}}|_{max} + |\lambda_{\tilde{C}}|_{max}\right) \\
& + 2\left(\left(\lambda_{max}^{v,thin}\right)_i + \left(\lambda_{max}^{v,thin}\right)_j + \left(\lambda_{max}^{v,thin}\right)_k\right)\Bigg] I \\
& + \tilde{A}^{+}_{i-1,j,k} + \tilde{B}^{+}_{i,j-1,k} + \tilde{C}^{+}_{i,j,k-1} \\
& + \left(\lambda_{max}^{v,thin}\right)_{i-1,j,k} + \left(\lambda_{max}^{v,thin}\right)_{i,j-1,k} + \left(\lambda_{max}^{v,thin}\right)_{i,j,k-1} \\
D = \Bigg[& \frac{1}{J\triangle\tau} + \alpha\left(|\lambda_{\tilde{A}}|_{max} + |\lambda_{\tilde{B}}|_{max} + |\lambda_{\tilde{C}}|_{max}\right) \\
& + 2\left(\left(\lambda_{max}^{v,thin}\right)_i + \left(\lambda_{max}^{v,thin}\right)_j + \left(\lambda_{max}^{v,thin}\right)_k\right)\Bigg] I \\
U = \Bigg[& \frac{1}{J\triangle\tau} + \alpha\left(|\lambda_{\tilde{A}}|_{max} + |\lambda_{\tilde{B}}|_{max} + |\lambda_{\tilde{C}}|_{max}\right) \\
& + 2\left(\left(\lambda_{max}^{v,thin}\right)_i + \left(\lambda_{max}^{v,thin}\right)_j + \left(\lambda_{max}^{v,thin}\right)_k\right)\Bigg] I \\
& - \tilde{A}^{-}_{i+1,j,k} - \tilde{B}^{-}_{i,j+1,k} - \tilde{C}^{-}_{i,j,k+1} \\
& - \left(\lambda_{max}^{v,thin}\right)_{i+1,j,k} - \left(\lambda_{max}^{v,thin}\right)_{i,j+1,k} - \left(\lambda_{max}^{v,thin}\right)_{i,j,k+1}
\end{aligned} \tag{2.39}$$

In above equations, $\tilde{A}^{\pm}_{i,j,k}$, $\tilde{B}^{\pm}_{i,j,k}$ and $\tilde{C}^{\pm}_{i,j,k}$ are flux jacobian ma-

trices, which are split to satisfy the diagonal dominance as follows:

$$\tilde{A}^{\pm}_{i,j,k} = \frac{1}{2}\left(\tilde{A} \pm \kappa |\lambda_{\tilde{A}}|_{max}\right) \tag{2.40}$$

κ in Eq. 2.40 is typically chosen between 1.01 and 1.05.

The viscous flux jacobian is replaced by the spectral radii of their thin layer approximation, which is written by $\lambda^{v,thin}_{max}$ in Eq. 2.39 , as suggested in [22]. The viscous spectral radius is determined as

$$\lambda^{v,thin}_{max} = \left(\frac{k\frac{\partial \rho_m}{\partial p}}{\frac{\partial \rho_m}{\partial T} + \frac{\partial h_m}{\partial T}\frac{\partial \rho_m}{\partial p}\rho_m - \frac{\partial h_m}{\partial p}\frac{\partial \rho_m}{\partial T}\rho_m} \right) \frac{\triangle S}{|\Omega|} \tag{2.41}$$

where $\triangle S$, denotes interfacial length or area, and $|\Omega|$ represents cell area or volume.

2.5 Equation of states

Applying ideal gas assumption on equation of states for water and liquid phase may give erroneous solution, because it has substantial mismatch near the saturation point. Furthermore, the temperature and pressure range shown in flow fields around TVC are wide, and hence, equation of states should be accurate over wide applicable temperature and pressure ranges. The IAPWS-97 formulation, which

satisfy these requirement among the various equation of states, is suitable selection. However, it is still open to improvement on computational efficiency, and hence SBTL model on IAPWS formulation is further presented in this section.

2.5.1 IAPWS formulation

IAPWS-97formulation computes the properties of each phase using the Gibbs free energy g, which is defined as a function of pressure and temperature. The formula for Gibbs free energy for liquid phase is

$$\frac{g(P,T)}{RT} = \gamma(\pi,\tau) = \sum_{i=1}^{34} n_i (7.1-\pi)^{I_i} (\tau - 1.222)^{J_i}, \qquad (2.42)$$

where $\pi = P/P^*$, $\tau = T^*/T$ with $P^* = 16.53$Mpa and $T^* = 1386$K. The coefficients n_i, I_i, and J_i of Eq. (2.42) are listed in table 1, and its valid temperature and pressure ranges are follows:

$$273.15K \leq T \leq 623.15K \quad , \quad P_s(T) \leq p \leq 100Mpa \quad (2.43)$$

It is noticeable that Eq. (2.42) also gives the reasonable value for metastable superheated-liquid region close to the saturation line.

For vapor phase, the formula of Gibbs free energy can be sub-

i	I_i	J_i	n_i	i	I_i	J_i	n_i
1	0	-2	0.14632971213167	18	2	3	$-0.44141845330846\times10^{-5}$
2	0	-1	−0.84548187169114	19	2	17	$-0.72694996297594\times10^{-15}$
3	0	0	$-0.37563603672040\times10^{1}$	20	3	-4	$-0.31679644845054\times10^{-4}$
4	0	1	$0.33855169168385\times10^{1}$	21	3	0	$-0.28270797958312\times10^{-5}$
5	0	2	−0.95791963387872	22	3	6	$-0.85205128120103\times10^{-9}$
6	0	3	0.15772038513228	23	4	-5	$-0.22425281908000\times10^{-5}$
7	0	4	$-0.16616417199501\times10^{-1}$	24	4	-2	$-0.65171222895601\times10^{-6}$
8	0	5	$0.81214629983568\times10^{-3}$	25	4	10	$-0.14341729937924\times10^{-12}$
9	1	-9	$0.28319080123804\times10^{-3}$	26	5	-8	$-0.40516996860117\times10^{-6}$
10	1	-7	$-0.60706301565874\times10^{-3}$	27	8	-11	$-0.12734301741641\times10^{-8}$
11	1	-1	$-0.18990068218419\times10^{-1}$	28	8	-6	$-0.17424871230634\times10^{-9}$
12	1	0	$-0.32529748770505\times10^{-1}$	29	21	-29	$-0.68762131295531\times10^{-18}$
13	1	1	$-0.21841717175414\times10^{-1}$	30	23	-31	$0.14478307828521\times10^{-19}$
14	1	3	$-0.52838357969930\times10^{-4}$	31	29	-38	$0.26335781662795\times10^{-22}$
15	2	-3	$-0.47184321073267\times10^{-3}$	32	30	-39	$-0.11947622640071\times10^{-22}$
16	2	0	$-0.30001780793026\times10^{-3}$	33	31	-40	$0.18228094581404\times10^{-23}$
17	2	1	$0.47661393906987\times10^{-4}$	34	32	-41	$-0.93537087292458\times10^{-25}$

Table 1: Coefficients of Gibbs free energy for liquid phase

divided into the subcooled- and metastable-state, and hence, the formula for computing the saturation pressure is firstly introduced. The saturation pressure is evaluated as

$$\frac{p_s(T)}{p^*} = \left[\frac{2C}{-b+(B^2-4AC)^{0.5}}\right]^4 \tag{2.44}$$

where $p^* = 1$ Mpa and

$$\begin{aligned} A &= \Theta^2 + n_1^2\Theta + n_2^s \\ B &= n_3^s\Theta^2 + n_4^s\Theta + n_5^s \\ C &= n_6^s\Theta^2 + n_7^s\Theta + n_8^s \end{aligned} \tag{2.45}$$

with

$$\Theta = T + \frac{n_9^s}{T - n_{10}^s} \tag{2.46}$$

The coefficients in Eq. 2.45 and Eq. (2.46) are summarized in table 2.

The subcooled- and metastable-states have the identical form of the Gibbs free energy, which is composed of the ideal-gas term γ^0 and residual term γ^r as

$$\frac{g(P,T)}{RT} = \gamma^0(\pi,\tau) + \gamma^r(\pi,\tau), \tag{2.47}$$

i	n_i^s	i	n_i
1	$0.11670521452767 \times 10^4$	6	$0.14915108613530 \times 10^2$
2	$-0.72421316703206 \times 10^6$	7	$-0.48232657361591 \times 10^4$
3	$-0.17073846940092 \times 10^2$	8	$0.40511340542057 \times 10^6$
4	$0.12020824702470 \times 10^5$	9	-0.23855557567849
5	$-0.32325550322333 \times 10^7$	10	$0.65017534844798 \times 10^3$

Table 2: Coefficients for calculating the saturation pressure

i	J_i^0	n_i	i	J_i^0	n_i
1^a	0	$-0.96927686500217 \times 10^1$	6	-2	$0.14240819171444 \times 10^1$
2^a	1	$0.10086655968018 \times 10^2$	7	-1	$-0.43839511319450 \times 10^1$
3	-5	$-0.56087911283020 \times 10^{-2}$	8	2	-0.28408632460772
4	-4	$0.71452738081455 \times 10^{-1}$	9	3	$0.21268463753307 \times 10^{-1}$
5	-3	-0.40710498223928			

Table 3: Ideal gas part coefficients of Gibbs free energy for gas phase

where

$$\gamma^0 = \ln \pi + \sum_{i=1}^{9} n_i^0 \tau^{J_i^0} \qquad , \qquad \gamma^r = \sum_{i=1}^{13} n_i \pi^{I_i} (\tau - 0.5)^{J_i}, \quad (2.48)$$

with $P^* = 1Mpa$ and $T^* = 540K$. The ideal-gas term, γ^0, can be expressed by 9 terms in both the subcooled- and metastable-state, and its coefficients are summarized in table 3. These coefficients are identical in both the subcooled and metastable states, except at n_1^0 and n_2^0. In the metastable state, $n_1^0 = -0.96937268393049 \times 10$, and $n_2^0 = 0.10087275970006 \times 10^2$ are used.

On the other hand, The coefficients of the residual component in

the subcooled state and metastable state are different. The coefficients in table 4 are used for the residual component of the subcooled gas phase, while in table 5 are used for the metastable gas phase.

With the computed Gibbs free energy, the specific volume ν and enthalpy h are evaluated as

$$\begin{aligned} \nu &= \left(\frac{\partial g}{\partial P}\right)_T = \pi\left(\gamma_\pi^0 + \gamma_\pi^r\right)\left(\frac{RT}{P}\right), \\ h &= g - T\left(\frac{\partial g}{\partial T}\right)_P = \tau\left(\gamma_\tau^0 + \gamma_\tau^r\right)RT \end{aligned} \tag{2.49}$$

2.5.2 SBTL method

Using the IAPWS-97 formulation as a equation of states can guarantee the reasonable computational costs, however, it is still open to improve the computational efficiency becuase it is composed of many polynomial terms. Recently, International Association for the Properties of Water and Steam(IAPWS) introduced SBTL method to satisfy this requirement. It firstly defines the node and knot, which store the properties such as density or enthalpy and their derivatives, respectively as Fig. 4. The bi-quadratic interpolation function is de-

i	I_i	j_i	n_i	i	I_i	j_i	n_i
1	1	0	$-0.17731742473213\times10^{-2}$	23	7	0	$-0.59059564324270\times10^{-17}$
2	1	1	$-0.17834862292358\times10^{-1}$	24	7	11	$-0.12621808899101\times10^{-5}$
3	1	2	$-0.45996013696365\times10^{-1}$	25	7	25	$-0.38946842435739\times10^{-1}$
4	1	3	$-0.57581259083432\times10^{-1}$	26	8	8	$0.11256211360459\times10^{-10}$
5	1	6	$-0.50325278727930\times10^{-1}$	27	8	36	$-0.82311340897998\times10^{1}$
6	2	1	$-0.33032641670203\times10^{-4}$	28	9	13	$0.19809712802088\times10^{-7}$
7	2	2	$-0.18948987516315\times10^{-3}$	29	10	4	$0.10406965210174\times10^{-18}$
8	2	4	$-0.39392777243355\times10^{-2}$	30	10	10	$-0.10234747095929\times10^{-12}$
9	2	7	$-0.43797295650573\times10^{-1}$	31	10	14	$-0.10018179379511\times10^{-8}$
10	2	36	$-0.26674547914087\times10^{-4}$	32	16	29	$-0.80882908646985\times10^{-10}$
11	3	0	$0.20481737692309\times10^{-7}$	33	16	50	0.10693031879409
12	3	1	$0.43870667284435\times10^{-6}$	34	18	57	−0.33662250574171
13	3	3	$-0.32277677238570\times10^{-4}$	35	20	20	$0.89185845355421\times10^{-24}$
14	3	6	$-0.15033924542148\times10^{-2}$	36	20	35	$0.30629316876232\times10^{-12}$
15	3	35	$-0.40668253562649\times10^{-1}$	37	20	48	$-0.42002467698208\times10^{-5}$
16	4	1	$-0.78847309559367\times10^{-9}$	38	21	21	$-0.59056029685639\times10^{-25}$
17	4	2	$0.12790717852285\times10^{-7}$	39	22	53	$0.37826947613457\times10^{-5}$
18	4	3	$0.48225372718507\times10^{-6}$	40	23	39	$-0.12768608934681\times10^{-14}$
19	5	7	$0.22922076337661\times10^{-5}$	41	24	26	$0.73087610595061\times10^{-28}$
20	6	3	$-0.16714766451061\times10^{-10}$	42	24	40	$0.55414715350778\times10^{-16}$
21	6	16	$-0.21171472321355\times10^{-2}$	43	24	58	$-0.94369707241210\times10^{-6}$
22	6	35	$-0.23895741934104\times10^{2}$				

Table 4: Residual part coefficients of Gibbs free energy for subcooled gas phase

i	I_i	J_i	n_i	i	I_i	J_i	n_i
1	1	0	$-0.73362260186506\times10^{-2}$	8	3	4	$-0.63498037657313\times10^{-2}$
2	1	2	$-0.88223831943146\times10^{-1}$	9	3	16	$-0.86043093028588\times10^{-1}$
3	1	5	$-0.72334555213245\times10^{-1}$	10	4	7	$0.75321581522770\times10^{-2}$
4	1	11	$-0.40813178534455\times10^{-2}$	11	4	10	$-0.79238375446139\times10^{-3}$
5	2	1	$0.20097803380207\times10^{-2}$	12	5	9	$-0.22888160778447\times10^{-3}$
6	2	7	$-0.53045921898642\times10^{-1}$	13	5	10	$-0.26456501482810\times10^{-2}$
7	2	16	$-0.76190409086970\times10^{-2}$				

Table 5: Residual part coefficients of Gibbs free energy for metastable gas phase

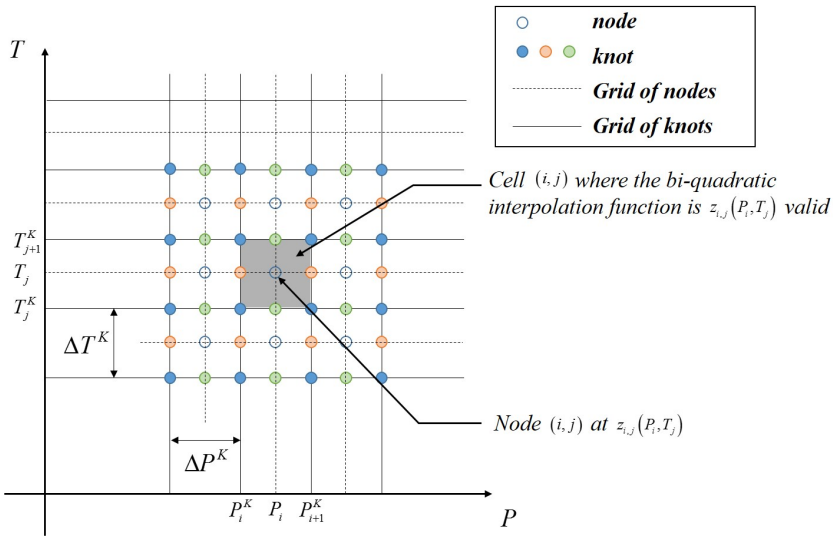

Figure 4: Definition of nodes and knots for bi-quadratic interpolation

fined as

$$z_{\{i,j\}}(P,T) = \sum_{k=1}^{3}\sum_{l=1}^{3} a_{ijkl}\left(P-P_i\right)^{k-1}\left(T-T_j\right)^{l-1} \tag{2.50}$$

where $z_{i,j}$ is an arbitrary dependent variable (density and enthalpy) in the cell $\{i,j\}$, and a_{ijkl} is the nine coefficients of the spline polynomial function valid in the cell $\{i,j\}$. The spline function interpolates values between a set of discrete data points, the so-called nodes. The nodes are defined at the midpoint between nodes along the p and T, respectively.

$$p_{i+1}^{K} = \frac{1}{2}\left(p_i + p_{i+1}\right), \qquad i = 1,...,imax-1 \tag{2.51}$$

$$T_{j+1}^{K} = \frac{1}{2}\left(T_j + T_{j+1}\right), \qquad j = 1,...,jmax-1 \tag{2.52}$$

The number of nodes and knots are chosen to ensure the desired accuracy of spline function over the full domain $[p_{min}, p_{max}]$ and $[T_{min}, T_{max}]$. The searching algorithm for node $\{i,j\}$ in interpolation process is simply made by distributing nodes equidistantly along p and T, so that indices i and j can be easily found by

$$i = floor\left(\frac{p-p_1^K}{\triangle p^K}\right) \qquad , \qquad j = floor\left(\frac{T-T_1^K}{\triangle T^K}\right) \tag{2.53}$$

where $\triangle p^K$ and $\triangle T^K$ are constant.

The nine coefficient a_{ijkl} in Eq. (2.50) are determined satisfying C^1 continuity across every data point:

- Each of polynomials $z_{\{i,j\}}$ intersect the value of node (i, j).

$$z_{\{i,j\}}(P_i, T_j) = z_{i,j} \qquad i = 1, ..., imax, \quad j = 1, ..., jmax$$

- The z values at the midpoints of the cell boundaries $\left(i^K, j\right)$, $\left(i^{K+1}, j\right)$, $\left(i, j^K\right)$ and $\left(i, j^{K+1}\right)$, marked as a green or orange color knot in Fig. (4), are equal to the corresponding values of the adjacent cells

$$z_{\{i,j\}}\left(p_{i+1}^K, T_j\right) = z_{\{i+1,j\}}\left(p_{i+1}^K, T_j\right)$$
$$i = 1, ..., imax - 1, \; j = 1, ..., jmax$$
$$z_{\{i,j\}}\left(p_i, T_{j+1}^K\right) = z_{\{i,j+1\}}\left(p_i, T_{j+1}^K\right)$$
$$i = 1, ..., imax, \; j = 1, ..., jmax - 1$$

- The derivatives $(\partial z/\partial p)_T$ at $\left(i^K, j\right)$ and $\left(i^{K+1}, j\right)$, as well as $(\partial z/\partial T)_p$ at $\left(i, j^K\right)$ and $\left(i, j^{K+1}\right)$, are equal to the correspond-

ing derivatives of the adjacent cells.

$$\left(\frac{\partial z}{\partial P}\right)_T\Bigg|_{\{i,j\}}\left(p^K_{i+1},T_j\right)=\left(\frac{\partial z}{\partial P}\right)_T\Bigg|_{\{i+,j\}}\left(p^K_{i+1},T_j\right)$$

$$i=1,...,imax-1,j=1,...,jmax$$

$$\left(\frac{\partial z}{\partial T}\right)_p\Bigg|_{\{i,j\}}\left(p_i,T^K_{j+1}\right)=\left(\frac{\partial z}{\partial T}\right)_p\Bigg|_{\{i,j+1\}}\left(p_i,T^K_{j+1}\right)$$

$$i=1,...,imax,j=1,...,jmax-1$$

- The z values and the cross derivatives $\left(\partial^2 z/\partial p\partial T\right)$ at the four corner knots, marked as a blue color knot in Fig. (4), are equal to the corresponding values of the neighboring cells

$$z_{\{i,j\}}\left(p^K_{i+1},T^K_j\right)=z_{\{i+1,j\}}\left(p^K_{i+1},T^K_j\right)$$

$$i=1,...,imax-1,j=1,...,jmax$$

$$z_{\{i,j\}}\left(p^K_{i+1},T^K_{j+1}\right)=z_{\{i+1,j\}}\left(p^K_{i+1},T^K_{j+1}\right)$$

$$i=1,...,imax-1,j=1,...,jmax$$

$$z_{\{i,j\}}\left(p^K_i,T^K_{j+1}\right)=z_{\{i,j+1\}}\left(p^K_i,T^K_{j+1}\right)$$

$$i=1,...,imax,j=1,...,jmax-1$$

$$z_{\{i,j\}}\left(p_{i+1}^K, T_{j+1}^K\right) = z_{\{i,j+1\}}\left(p_{i+1}^K, T_{j+1}^K\right)$$

$$i = 1, ..., imax, j = 1, ..., jmax - 1$$

$$\left(\frac{\partial^2 z}{\partial p \partial T}\right)\Bigg|_{i,j}\left(p_{i+1}^K, T_j^K\right) = \left(\frac{\partial^2 z}{\partial p \partial T}\right)\Bigg|_{i+1,j}\left(p_{i+1}^K, T_j^K\right)$$

$$i = 1, ..., imax - 1, j = 1, ..., jmax$$

$$\left(\frac{\partial^2 z}{\partial p \partial T}\right)\Bigg|_{i,j}\left(p_{i+1}^K, T_{j+1}^K\right) = \left(\frac{\partial^2 z}{\partial p \partial T}\right)\Bigg|_{i+1,j}\left(p_{i+1}^K, T_{j+1}^K\right)$$

$$i = 1, ..., imax - 1, j = 1, ..., jmax$$

$$\left(\frac{\partial^2 z}{\partial p \partial T}\right)\Bigg|_{i,j}\left(p_i^K, T_{j+1}^K\right) = \left(\frac{\partial^2 z}{\partial p \partial T}\right)\Bigg|_{i,j+1}\left(p_i^K, T_{j+1}^K\right)$$

$$i = 1, ..., imax - 1, j = 1, ..., jmax$$

$$\left(\frac{\partial^2 z}{\partial p \partial T}\right)\Bigg|_{i,j}\left(p_{i+1}^K, T_{j+1}^K\right) = \left(\frac{\partial^2 z}{\partial p \partial T}\right)\Bigg|_{i,j+1}\left(p_{i+1}^K, T_{j+1}^K\right)$$

$$i = 1, ..., imax - 1, j = 1, ..., jmax$$

- At the outer boundaries of the grid of knots, the following analytical values are provided

$$\left(\frac{\partial z}{\partial p}\right)_T\Bigg|_{\{1,j\}}\left(p_1^K, T_j\right) = \left(\frac{\partial z}{\partial p}\right)_T\left(p_1^K, T_j\right) \qquad j = 1, ..., jmax$$

$$\left(\frac{\partial z}{\partial p}\right)_T\Bigg|_{\{imax,j\}}\left(p_{imax+1}^K, T_j\right) = \left(\frac{\partial z}{\partial p}\right)_T\left(p_{imax+1}^K, T_j\right)$$

$$j = 1, ..., jmax$$

$$\left(\frac{\partial z}{\partial T}\right)_p\Bigg|_{\{i,1\}}\left(p_i,T_1^K\right)=\left(\frac{\partial z}{\partial T}\right)_p\left(p_i,T_1^K\right)\qquad i=1,...,imax$$

$$\left(\frac{\partial z}{\partial T}\right)_p\Bigg|_{\{i,jmax\}}\left(p_i,T_{jmax+1}^K\right)=\left(\frac{\partial z}{\partial T}\right)_p\left(p_i,T_{jmax+1}^K\right)$$

$$i=1,...,imax$$

$$\left(\frac{\partial^2 z}{\partial p\partial T}\right)\Bigg|_{\{1,1\}}\left(p_1^K,T_1^K\right)=\left(\frac{\partial^2 z}{\partial p\partial T}\right)\left(p_1^K,T_1^K\right)$$

$$\left(\frac{\partial^2 z}{\partial p\partial T}\right)\Bigg|_{\{imax,1\}}\left(p_{imax+1}^K,T_1^K\right)=\left(\frac{\partial^2 z}{\partial p\partial T}\right)\left(p_{imax+1}^K,T_1^K\right)$$

$$\left(\frac{\partial^2 z}{\partial p\partial T}\right)\Bigg|_{\{1,jmax\}}\left(p_1^K,T_{jmax+1}^K\right)=\left(\frac{\partial^2 z}{\partial p\partial T}\right)\left(p_1^K,T_{jmax+1}^K\right)$$

$$\left(\frac{\partial^2 z}{\partial p\partial T}\right)\Bigg|_{\{imax,jmax\}}\left(p_{imax+1}^K,T_{jmax+1}^K\right)$$

$$=\left(\frac{\partial^2 z}{\partial p\partial T}\right)\left(p_{imax+1}^K,T_{jmax+1}^K\right)$$

The coefficients satisfying above conditions are stored before computation for each sub cells, and then computes properties with 9 coefficients directly. The table 6 shows elapsed time for validation problems and pressure L2 norm with IAPWS formulation and SBTL method. As observed, implemented SBTL method can save the computational cost about 2.8 times better than IAPWS-97 formulation with reasonable error. Therefore, SBTL method will be applied as equation of states for following validation and TVC computations.

Test case	EOS	Computational cost (sec)	Efficiency (IAPWS/SBTL)	Pressure L2 norm
Moore B	IAPWS	6,386	2.80	2.10×10^{-6}
	SBTL	2,283		
Moore C	IAPWS	5,298	2.71	2.38×10^{-6}
	SBTL	1,955		

Table 6: Computed computational efficiency for validation cases

2.6 Turbulence model

The adequate turbulence model should be employed to take into account the turbulence effect within the framework of Reynolds Averaged Navier-Stokes formulation. Among the various turbulence models, $k-\omega$ SST model proposed by Menter is applied in this research with compressibility correction. It is composed of two trasport equations of turbulent kinetic energy k and the dissipation rate ω.

2.6.1 The Menter's $k-\omega$ SST turbulence model

Among the two-equation turbulence model, $k-\omega$ model [23] is superior to the $k-\varepsilon$ model [24] within the laminar sublayer because it doesn't need damping function allowing simple Dirichlet boundary conditions. This simplicity gives additional virtue in superior numerical stability to the other models. Furthermore, $k-\omega$ model shows

better accuracy than $k-\varepsilon$ model in logarithmic part of the boundary layer for flow fields containing adverse pressure gradient. However, $k-\omega$ model has been shown to be inappropriate for wake region of boundary layer, because it is sensitive to freestream value of ω [25].

On the other hand, behavior of $k-\varepsilon$ model is superior to that of $k-\omega$ model in the wake regions of boundary layer. Even though no turbulence models seem to be suitable for all free shear flows (such as wake, jet, mixing layer), $k-\varepsilon$ model is still to be a fair compromise. However, it suffers from numerical instabilities in the inner region of the boundary layer.

To incorporate positive features of both turbulence models, Menter suggested $k-\omega$ SST turbulence model, which combines $k-\omega$ model and transformed $k-\varepsilon$ model via blending function F_1. The transport equation for turbulent kinetic energy and the dissipation rate in integral form is

$$\frac{\partial}{\partial \tau}\int_{\Omega}\mathbf{W_T}d\Omega+\oint_{\partial\Omega}\left[(\mathbf{F_{c,T}}-\mathbf{F_{v,T}})\cdot\mathbf{n}\right]dS=\int_{\Omega}\mathbf{D_T}d\Omega \qquad (2.54)$$

The vector for conservative variable vector for turbulent variables $\mathbf{W_T}$

is

$$\mathbf{W_T} = \begin{bmatrix} \rho_m K \\ \rho_m \omega \end{bmatrix} \tag{2.55}$$

and conservative flux tensor $\mathbf{F_{c,T}}$ is

$$\mathbf{F_{c,T}} = \begin{bmatrix} \rho_m K u & \rho_m K v & \rho_m K w \\ \rho_m \omega u & \rho_m \omega v & \rho_m \omega w \end{bmatrix} \tag{2.56}$$

The viscous flux tensor $\mathbf{F_{v,T}}$ is given by

$$\mathbf{F_{v,T}} = \begin{bmatrix} (\mu_L + \sigma_K \mu_T)\frac{\partial K}{\partial x} & (\mu_L + \sigma_K \mu_T)\frac{\partial K}{\partial y} & (\mu_L + \sigma_K \mu_T)\frac{\partial K}{\partial z} \\ (\mu_L + \sigma_\omega \mu_T)\frac{\partial \omega}{\partial x} & (\mu_L + \sigma_\omega \mu_T)\frac{\partial \omega}{\partial y} & (\mu_L + \sigma_\omega \mu_T)\frac{\partial \omega}{\partial z} \end{bmatrix} \tag{2.57}$$

The source term on kinetic energy and dissipation rate are defined as

$$\mathbf{W_T} = \begin{bmatrix} \tilde{P} - \beta_T^* \rho \omega K \\ \frac{C\omega}{\nu_T}\tilde{P} - \beta_T \rho \omega^2 + 2\rho(1-F_1)\sigma_{\omega 2}\frac{1}{\omega}\frac{\partial k}{\partial x_i}\frac{\partial \omega}{\partial x_i} \end{bmatrix} \tag{2.58}$$

Note that it is generally recommended to employ the production limiter to prevent developing turbulence in stagnation regions as follows:

$$\tilde{P} = min\left(\tau_{ij}^F S_{ij}, 10\beta_T^* \rho K \omega\right) \tag{2.59}$$

where τ_{ij}^F is the turbulent stress based on Boussinesq eddy-viscosity

hypothesis

$$\tau_{ij}^{F} = 2\mu_T S_{ij} - \frac{2}{3}\mu_T \frac{\partial u_i}{\partial x_i}\delta_{ij} - \frac{2}{3}\rho K \delta_{ij} \tag{2.60}$$

With computed turbulent variables, turbulent viscosity μ_T is evaluated by

$$\mu_T = \frac{a_1 \rho_m K}{max\left(a_1\omega, F_2\sqrt{2S_{ij}S_{ij}}\right)} \tag{2.61}$$

where strain rate tensor S_{ij} in Eq. (2.60) and Eq. (2.61) is defined by

$$S_{ij} = \frac{1}{2}\left(\frac{\partial u_i}{\partial x_j} + \frac{\partial u_j}{\partial x_i}\right) \tag{2.62}$$

The blending function F_1 plays a major role in switching from $K-\omega$ model for boundary layer to $K-\varepsilon$ model for free shear layer, and it is defined as follows:

$$F_1 = tanh\left(arg_1^4\right) \tag{2.63}$$

$$arg1 = min\left[max\left(\frac{\sqrt{K}}{0.09\omega d}, \frac{500\mu_L}{\rho\omega d^2}\right), \frac{4\rho\sigma_{w2}K}{CD_{k\omega}d^2}\right] \tag{2.64}$$

$$CD_{k\omega} = max\left(2\frac{\rho\sigma_{\omega 2}}{\omega}\frac{\partial K}{\partial x_i}\frac{\partial \omega}{\partial x_i}, 10^{-10}\right) \tag{2.65}$$

$$F_2 = tanh\left(arg_2^2\right) \tag{2.66}$$

$$arg2 = max\left(\frac{2\sqrt{K}}{\beta_T^*\omega d}, \frac{500\nu_L}{\omega d^2}\right) \tag{2.67}$$

by imposing d in Eq. (2.64$\sim$2.68) as the distance between the cell center point and the nearest wall.

The coefficients in this section β_T, C_ω, σ_K and σ_ω are computed with blending function F_1 and coefficients of each turbulence models as follows:

$$\phi^T = F_1 \phi_1^T + (1 - F_1)\, \phi_2^T \tag{2.68}$$

where subscript 1 and 2 denote coefficient of $k-\omega$ and $k-\varepsilon$ model respectively.

The coefficients of $k-\omega$ model are given by

$$\beta_1^T = 0.075 \quad , \quad C_{\omega 1} = 5/9 \quad , \quad \sigma_{K1} = 0.85 \quad , \quad \sigma_{\omega 1} = 0.5 \tag{2.69}$$

and the coefficients of $k-\varepsilon$ model are given by

$$\beta_1^T = 0.0828 \quad , \quad C_{\omega 1} = 0.44 \quad , \quad \sigma_{K1} = 1.0 \quad , \quad \sigma_{\omega 1} = 0.856 \tag{2.70}$$

The boundary conditions and freestream values typically used as follows:

$$\frac{U_\infty^2}{10^5 Re_L} < K_{farfield} < \frac{U_\infty^2}{10 Re_L} \tag{2.71}$$

$$\frac{U_\infty}{L_{farfield}} < \omega_{farfield} < \frac{10 U_\infty}{L_{farfield}} \tag{2.72}$$

$$K_{wall} = 0 \tag{2.73}$$

$$\omega_{wall} = \frac{60\mu}{\beta_1^T \rho_m d^2} \tag{2.74}$$

2.6.2 Compressibility correction

The flow field in TVC contains the complex compressible physics such as shock-train, and hence compressibility correction for turbulence model is additionally considered. Among the various compressibility corrections, the model suggested by Sarkar *et al.* [26] is used in this research. This correction suggests simply adding the compressible dissiaption ε_c, and pressure dilatation term $\overline{p"d"}$ in turbulent kinetic equation of $k-\varepsilon$ model. Each terms are defined by

$$\varepsilon_c = \gamma_1 M_t^2 \varepsilon \tag{2.75}$$

$$\overline{p"d"} = -\gamma_2 \tilde{P} M_t^2 + \gamma_3 \rho \varepsilon M_t^2 \tag{2.76}$$

where turbulent Mach number M_t is defined by

$$M_t = \sqrt{\frac{2K}{c^2}} \tag{2.77}$$

The following values are suggested based on DNS computation for coefficients as

$$\gamma_1 = 1.0 \quad , \quad \gamma_2 = 0.4 \quad \textit{and} \quad \gamma_3 = 0.2 \tag{2.78}$$

2.7 Phase-changing models

Two types of phase-changing models are considered in the present work. The first is based on the classical nucleation theory, which is commonly adopted for condensing nozzles or low-pressure steam turbines [27–29], and the other one is based on the Hertz–Knudsen equation that is widely used for cavitation or boiling problems [30–32]. Both models incorporate the phase-changing phenomenon as non-equilibrium process, but the Hertz-Knudsen equation-based model does not reflect the effect of droplet distrubution. Detailed descriptions on both models are followed in subsections.

2.7.1 Nucleation model

2.7.1.1 Critical droplet radius

The reversible work required to form a single spherical droplet of radius r from a supersaturated vapor is considered to be equal

to Gibbs free energy during the process of formation. The classical Gibbs free energy is composed with following portions:

1. The Formation of the first 'n' molecules from the superheated steam. There is no change in free energy during this process

$$\triangle G_1 = 0 \tag{2.79}$$

2. Isothermal expansion of steam from pressure P to saturation pressure $P_s(T_v)$

$$\triangle G_2 = \frac{4}{3}\pi r^3 \rho_l \int_P^{P_s} \frac{1}{\rho_v} dp = -\frac{4}{3}\pi r^3 \rho_l R T_v ln S \tag{2.80}$$

where S is the supersaturation ratio defined as $S = P/P_{sat}(T_v)$

3. This portion is related with condensation of vapor at saturation pressure P_{sat} and constant temperature T into bulk liquid phase, and creation of a flat surface. However, it can be neglected if we assume the equilibrium process in condensation phenomena, because their chemical potentials are equal

$$\triangle G_3 = 0 \tag{2.81}$$

4. Formation of droplets of radius 'r' and surface area $4\pi r^2$ from bulk liquid yields

$$\triangle G_4 = 4\pi r^2 \sigma \tag{2.82}$$

where σ is the surface tension of the shperical liquid droplets. This portion, Eqn. (2.82), is the capillarity approximation, and there were many debates on its definition.

5. Isothermal compression from the saturation pressure P_{sat} to the vapor pressure P gives

$$\triangle G_5 = \frac{4}{3}\pi r^3 \left(P - P_{sat}\right) \tag{2.83}$$

This portion is generally neglected because of small magnitude comparing to other portions.

As a result, overall Gibbs free energy is expressed as

$$\triangle G = 4\pi r^2 \sigma - \frac{4}{3}\pi \rho_l R T_v ln S \tag{2.84}$$

The Gibbs free energy is increased as droplet radius r is grown as Fig. 5 for superheated vapor, and thus probability of droplet formulation is reduced, while it has certain maximum value $\triangle G^*$ with r^* termed as the Kelvin-Helmholtz or critical droplet radius for su-

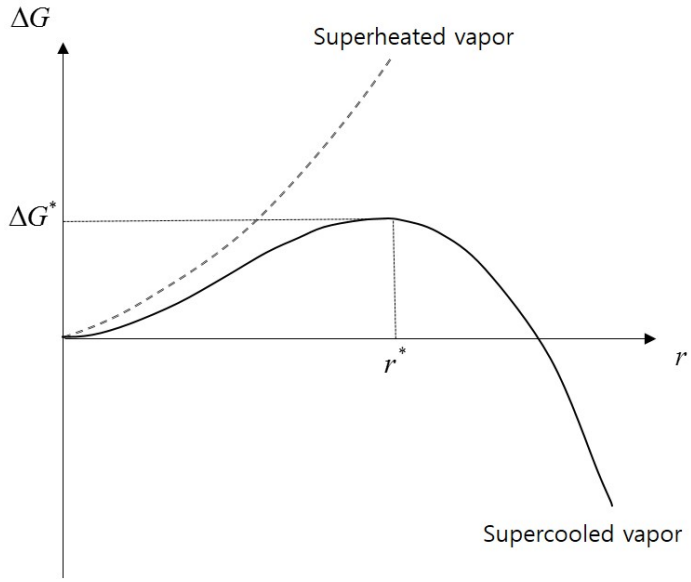

Figure 5: Schematic diagram showing the variation of Gibbs free energy $\triangle G$ with droplet radius r

percooled vapor. In supercooled status, a droplet with $r > r^*$ reduces the free energy of system by capturing molecules, and has a tendency grow, while droplet with $r < r^*$ is evaporated.

An expression for critical radius r^* is obtained by differentiating Eqn. (2.84) with respect to r and equating to zero, hence

$$r^* = \frac{2\sigma}{\rho_l RT\, ln\,(S)}, \tag{2.85}$$

and

$$\triangle G_* = \frac{4\pi r_*^2 \sigma}{3} = \frac{16\pi\sigma^3}{3\left(\rho_l RT_v lnS\right)^2} \tag{2.86}$$

In onset of nucleation, newly generated droplet has a radius equal to Eqn. (2.85), and increasing the supersaturation ratio S reduces this radius as well as activation barrier $\triangle G^*$. It also means the increment of probability in triggering the nucleation. A droplet of radius r comprising g molecules is called a g-mer. If m is the mass of a molecule, the droplet mass and surface area are expressed as $4/3\pi r^3\rho_l = gm$ and $4\pi r^2 = Ag^{2/3}$ respectively, where $A^3 = 36\pi\,(m/\rho_l)^2$. Substituting these relation into Eqn. (2.84) gives the formula of Gibbs free energy $\triangle G$ in terms of g as

$$\frac{\triangle G}{K_b T_v} = \frac{A\sigma}{K_b T_v} g^{2/3} - glnS \tag{2.87}$$

where K_b is the Boltzmann's constant.

2.7.1.2 Nucleation rate

The net rate per unit volume I_g at which g-mers grow to $(g+1)$ -mers is termed as the nucleation current and is expressed as

$$I_g = C_g f_g - E_{g+1} f_{g+1} \tag{2.88}$$

where C_g is the rate at which a g-mer acquires a molecule(condensation rate), E_{g+1} is the rate at which a $(g+1)$-mer loses a molecule(evaporation

rate), and f_g is the concentration of g-mers under the favorable condition for nucleation. Assuming that clusters can be modeled as spherical droplets down to the smallest sizes

$$C_g = q_c A g^{2/3} \frac{\rho_v \bar{v}_v}{4m} = q_c A g^{2/3} \frac{P}{\sqrt{2\pi m K_b T_v}} \tag{2.89}$$

where $\bar{v}_v$ is the mean speed of vapor molecules and q_c is the condensation coefficient, the fraction of molecules incident on the surface that are absorbed into the droplet. On the other hand, E_{g+1} has a following relation to satisfy the principle of balance as

$$C_g n_g = E_{g+1} n_{g+1} \tag{2.90}$$

Then, the time rate of change for the concentration of g-mers is given by

$$\begin{aligned} \frac{\partial f_g}{\partial t} &= -\left[\left(C_g f_g - E_{g+1} f_{g+1}\right) - \left(C_{g-1} f_{g-1} - E_g f_g\right)\right] \\ &= -\left(I_g - I_{g-1}\right) \cong -\frac{\partial I_g}{\partial g} \end{aligned} \tag{2.91}$$

Before solving the Eqn. (2.91), Eqn. (2.88) is simplified by eliminat-

ing E_{g+1} with relation expressed in Eqn. (2.90), and it yields

$$\frac{I_g}{C_g n_g} = \frac{f_g}{n_g} - \frac{f_{g+1}}{n_{g+1}} \cong -\frac{\partial}{\partial g}\left(\frac{f_g}{n_g}\right) \tag{2.92}$$

Eliminating I_g from Eqn. (2.91) and (2.92), the time rate of change of g-mer concentration is thus approximated in differential form as follows:

$$\frac{\partial f_g}{\partial t} = -\frac{\partial I_g}{\partial g} = \frac{\partial}{\partial g}\left[C_g n_g \frac{\partial}{\partial g}\left(\frac{f_g}{n_g}\right)\right] \tag{2.93}$$

Equation (2.93) is the governing differential equation describing isothermal nucleation, and its solution has been studied under two seprate sets of conditions, transient solution and steady solution. Kashchiev [33] investigated the solution of Eqn. (2.93) in transient in terms of a characteristic time τ. If a given supersaturation is imposed on a vapor initially in a saturated condition, then I_g reaches 99% of its steady state value within a characteristic time of 10^{-7} to 10^{-6} seconds. However, this time scale is very short in comparison with overall time for common problems, transient solution is usually neglected, and thus steady state solution is generally adopted.

For steady solution, Eqn. (2.92) is integrated as

$$I_{CL}\int_{g=1}^{\infty} \frac{dg}{C_g n_g} = \int_{g=1}^{\infty} -d\left(\frac{f_g}{n_g}\right) \tag{2.94}$$

where I_{CL} is the classical steady state value of I. Before evaluating the integral on the right-hand side, it should be noted that $f_g/n_g \to 1$ for $g \to 1$ and $f_g/n_g \to 0$ for $g \to \infty$. Therefore

$$I_{CL} = \left[\int_{g=1}^{\infty} \frac{dg}{C_g n_g} \right]^{-1} \tag{2.95}$$

In supercooled vapor state, small liquid clusters are continuously being formed and disrupted by the molecular collision process even in unfeasible flow condition for microscopic nucleation phenomena. The individual clusters are changed in all the time, but the size distribution can be assumed to be steady condition. By minimizing the free energy of the total vapor-droplet size, the number distribution of g-mers per volume in steady state follows the Boltzmann law as:

$$n_g \cong n_1 exp\left(-\frac{\triangle G}{K_b T_v} \right) \tag{2.96}$$

where n_1 is the numbers per unit volume of monomers. Substituting Eqn. (2.96) into Eqn. (2.95) yields

$$I_{CL} = \left[\int_{g=1}^{\infty} \frac{1}{C_g n_1 exp\left(\frac{-\triangle G}{K_b T_v} \right)} dg \right]^{-1} \tag{2.97}$$

C_g is proportional to $g^{2/3}$, which is slowly varying function with g-mer as compared to the rapidly changing exponential term in the denominator of Eqn. (2.97). C_g is thus approximated as C_{g*}, and Taylor series expansion on $\triangle G$ about $g*$ gives

$$\triangle G = \triangle G_* + (g - g_*)\left(\frac{\partial \triangle G}{\partial g}\right)_* + \frac{(g-g_*)^2}{2}\left(\frac{\partial^2 \triangle G}{\partial g^2}\right) + ... \tag{2.98}$$

Trucating after second-order term and noting that $(\partial \triangle G/\partial g)_* = 0$, Eqn. (2.97) becomes

$$I_{CL} = C_{g*} n_1 Z exp\left(\frac{-\triangle G_*}{K_b T_v}\right) \tag{2.99}$$

where Z is the so-called Zeldovich factor, given by

$$\begin{aligned} \frac{1}{Z} &= \int_{g=1}^{\infty} exp\left[-\left(\frac{\partial^2 \triangle G}{\partial g^2}\right)_* \frac{(g-g_*)^2}{2K_b T_v}\right] dg \\ &\cong \left[\frac{-\left(\frac{\partial^2 \triangle G}{\partial g^2}\right)_*}{2\pi K_b T_v}\right]^{-\frac{1}{2}} \end{aligned} \tag{2.100}$$

The term $\left(\frac{\partial^2 \triangle G}{\partial g^2}\right)_*$ in Eqn. (2.100) is evaluated with the definition of Gibbs free energy in terms of g in Eqn. (2.87), and final expression on nucleation rate can be summarized with Eqn. (2.89)

as:

$$I_{CL} = \frac{q_c}{1+\theta}\left(\frac{\rho_v^2}{\rho_l}\right)\sqrt{\frac{2\sigma}{\pi M^3}}\exp\left(-\frac{4}{3}\frac{\pi r^{*2}\sigma}{K_b T}\right). \tag{2.101}$$

In Eq. (2.101), q_c is the condensation coefficient, σ is the liquid surface tension, M is the mass of one molecule, r^* is the critical droplet radius, and K_b is the Boltzmann constant. θ is the non-isothermal correction factor defined by Kantrowicz [34] as

$$\theta = q_c\frac{2(\gamma-1)}{\gamma+1}\frac{h_{lv}}{RT}\left(\frac{h_{lv}}{RT}-\frac{1}{2}\right). \tag{2.102}$$

2.7.1.3 Droplet growth rate

Onset of nucleation, newly generated droplet with critical radius may grow as the vapor molecules condense further on their surface. Then, mass flux towards the droplet and net flux of energy(release of latent heat) to the vapor surroundings are occurred, which are commonly regarded as characteristic behavior of the droplet growth process. This transition if closely associated with Knudsen number(Kn), which is defined as the ratio of mean free path of the vapor molecules to the droplet size as follows:

$$Kn = \frac{\tilde{l}}{2r} \tag{2.103}$$

where r denotes the droplet radius, and $\tilde{l}$ is the mean free path of vapor molecules given by

$$\tilde{l} = \frac{3\mu_v}{P}\sqrt{\frac{\pi R T_v}{8}} \tag{2.104}$$

In Eqn. (2.104), mu_v is the dynamic viscosity of the vapor.

The Knudsen number plays a key role in determining the heat transfer coefficient, because the droplets can have wide range of radius during the condensation process. For very small Knudsen number ($Kn \ll 1$), applying the continuum hypothesis is adequate and the transfer process will be governed by diffusion. On the other hand, for large Knudsen number ($Kn \gg 1$), kinetic gas theory is applicable because of rarefied gas effects, and the process is governed by kinetic process of impingement of the vapor molecules to droplets. Despite the numerous researches have been conducted for droplet growth models to account for different regimes of Knudsen number, the model recognized as universal standard has not been formulated. Among these models, the Langmuir model is gathering the specific attention because it takes into account both continuum and rarefied gas effects. In order to formulate the growth rate of droplets, accounting the relation between mass and energy is important, and it thus

expressed as:

$$m\frac{dh_p}{dt} = -\left(h_v - h_l\right)\dot{M} - \dot{Q} \tag{2.105}$$

The term on left hand side is related to sensible heating and usually neglected due to its small amplitude. The first term on the right hand side is the latent heat energy to be removed in condensation process, and second term is the convective heat transfer rate $\dot{Q}$.

The mass transfer rate $\dot{M}$ is given by

$$\frac{dm_p}{dt} = -\dot{M} \tag{2.106}$$

where m_p is the mass of a single spherical droplet expressed as

$$m_p = \frac{4}{3}\pi r^3 \rho_l \tag{2.107}$$

Substituting Eqn. (2.106) and (2.107) into Eqn. (2.105),

$$\left(h_v - h_l\right)\frac{dm_p}{dt} = 4\pi r^2 K_v \left(T_l - T_v\right) \tag{2.108}$$

where $\left(h_v - h_l\right)\frac{dm_p}{dt}$ is the rate of latent heat to be removed during the condensation process. A part of this latent heat is convected to the vapor surrounding, while the remaining part is consumed to raise the

droplet temperature. In above equation, T_l represents the temperature of liquid phase and is assumed to be equal to the saturation temperature T_{sat} at the corresponding vapor pressure. K_v is the heat transfer coefficient. It can be simplified by substituting m_p as

$$\frac{dr}{dt} = Kv\frac{(T_{sat} - T_v)}{(h_v - h_l)\,\rho_l} \tag{2.109}$$

For the onset of nucleation, generated droplet radius is small, and hence heat transfer coefficient K_v should be modified to reflect the effect of Knusen number. Gyarmathy [35] has accounted this effect by

$$K_v = \frac{Nu\lambda_v}{2r} = \frac{\lambda_v}{r(1 + cKn)} \tag{2.110}$$

The constant c in above expression was proposed by White and Young [36] to improve the agreement with experimental data at low pressure, and has order of unity.

Applying Eqn. (2.110) into the Eqn. (2.109) with definition of Nusselt number gives the final expression on droplet growth rate

$$\frac{dr}{dt} = \frac{1}{\rho_l}\frac{\lambda_v}{(1 + 3.18Kn)}\frac{(T_{sat} - T_v)}{(h_v - h_l)}\frac{r - r^*}{r^2} \tag{2.111}$$

Above equation is termed Gyarmathy's droplet growth equation. There

is another expression given by Hill [37] as

$$(h_v - h_l)\,\rho_l \frac{dr}{dt} = \dot{Q} = \frac{P}{\sqrt{2\pi r T_v}} \frac{\gamma+1}{2\gamma} (T_{sat} - T_v) \tag{2.112}$$

Rearranging above equation yields

$$\frac{\partial r}{\partial t} = \frac{P}{(h_v - h_l)\,\rho_l \sqrt{2\pi R T}} \frac{\gamma+1}{2\gamma} C_p (T_d - T), \tag{2.113}$$

where T_d is droplet temperature that is substituted saturation temperature in Eqn. (2.112) to account the temperature variation with droplet radius as

$$T_d = T_{sat}(P) - [T_{sat}(P) - T] \frac{r^*}{r}. \tag{2.114}$$

2.7.1.4 Nucleation model

In preceding subsections, nucleation rate for newly generated droplets and growth rate for existing droplets are defined. Then, the phase-changing source term in nucleation model can be formulated

as follows:

$$S_{phase} = \frac{1}{J}\begin{bmatrix} 0 \\ 0 \\ 0 \\ 0 \\ 0 \\ -\left(\dot{m}_{nucleation} + \dot{m}_{growth}\right) \\ \rho_m I_{CL} \end{bmatrix}, \tag{2.115}$$

where

$$\dot{m}_{nucleation} = \frac{4}{3}\pi\rho_l I r^{*3}\,,\ \dot{m}_{growth} = 4\pi\rho_l r^2 \eta \frac{\partial r}{\partial t}. \tag{2.116}$$

Here, $\dot{m}_{nucleation}$ and $\dot{m}_{growth}$ indicate the contribution of the formation of new nuclei and the growth/decay of existing droplets according to the mass-changing rate, respectively. The nucleation rate I_{CL} is given in Eqn. (2.101), and droplet growth rate is given in Eqn. (2.111) or (2.113).

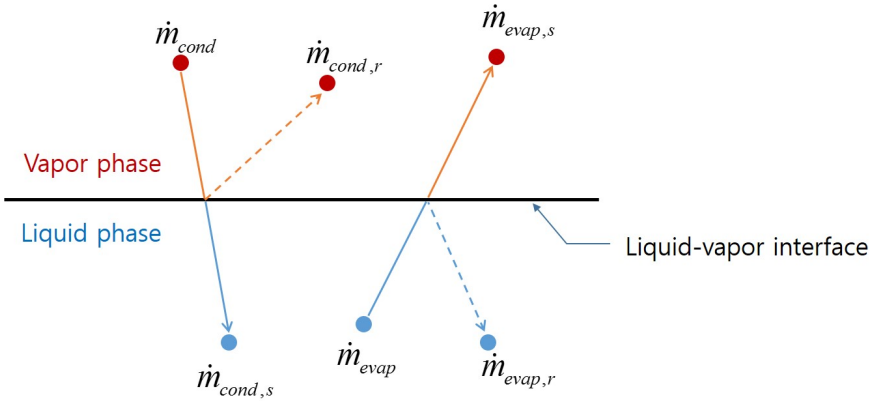

Figure 6: Description on phase-changing process in Hertz-Knudsen equation

2.7.2 Hertz-Knudsen equation based-model

The phase-changing process in Hertz-Knudsen equation-based model is explained from interfacial exchange of molecules as Fig. 6. The change of molecular phase through the interface is occurred when local pressure exceeds or drops the threshold value, which is generally considered as saturation pressure. When local pressure exceeds saturation pressure, some portions of vapor molecules passes the phase-interface by changing its foam into the liquid phase, however, some portions are reflected back to origin phase. Conversely, some portion of liquid molecules changes its foam into the vapor molecules when local pressure drops below the saturation pressure, while another portions are transferred back to liquid phase. There-

fore, molar exchanges in phase-change phenoemena is summarized as

$$\dot{m}_{cond} = \dot{m}_{cond,s} + \dot{m}_{cond,r} \tag{2.117}$$

$$\dot{m}_{evap} = \dot{m}_{evap,s} + \dot{m}_{evap,r} \tag{2.118}$$

where $\dot{m}_{cond}$ and $\dot{m}_{evap}$ denote phase-changing rate by condensation and evaporation, and the subscripts 's' and 'r' represent exchanged and reflected portion in phase-changing process, respectively.

The major contributions made by Hertz and Knudsen is defining mass changing rate in phase-changing phenomena based on kinetic theory of gases. According to their definition, the rate of evaporation depends on the liquid pressure and temperature, and conversely, the rate of condensation is depends on vapor pressure and temperature. They also proposed that the amount of exchange is estimated according to a half range Maxwellian distribution. As a result, the Hertz-Knudsen equation is stated as:

$$\dot{m} = \sqrt{\frac{M}{2\pi R}} \left\{ C_c \left(\frac{P_v}{\sqrt{T_v}} \right) - C_e \left(\frac{P_{sat}(T_l)}{\sqrt{T_l}} \right) \right\} \tag{2.119}$$

In Eqn. (2.119), C_e and C_c are the accomodation coefficients for evap-

oration and condensation, respectively. The accomodation coefficient for evaporation denotes the fraction of liquid molecules which passes through the phase-interface in evaporation process. Similarly, the accomodation coefficient for condensation represents the fraction of vapor molecules which get condensed upon striking the phase-interface in condensation process. The subscripts 'v' and 'l' refer the properties in vapor and liquid phase, respectively.

The governing equation, however, assumes the thermodynamic equilibrium which considers the identical pressure and temperature for liquid and vapor phase in computational cells. Therefore, the mass-changing rate in Hertz-Knudsen equation-based model in this research is summarized as follows:

$$S_{phase} = \frac{1}{J} \begin{bmatrix} 0 \\ 0 \\ 0 \\ 0 \\ 0 \\ \dot{m}_{evap} - \dot{m}_{cond} \\ 0 \end{bmatrix}, \tag{2.120}$$

and

$$\dot{m}_{evap} = C_{evap} \frac{max(P_{sat} - P, 0)}{\sqrt{2\pi RT}} \rho_l \alpha_l, \tag{2.121}$$

$$\dot{m}_{cond} = C_{cond} \frac{max(P - P_{sat}, 0)}{\sqrt{2\pi RT}} \rho_g \alpha_g. \tag{2.122}$$

Here, P_{sat} and α represent the saturation pressure and volume fraction for each phases, respectively.

C_{evap} and C_{cond} are empirical coefficients from accomodation coefficients to adjust the changing rate for evaporation and condensation. There are many experimental investigations to identify these empirical coefficients, for example, by Cammenga, Eames *et al.*, Bedeaux *et al.* and Marek *et al.* However, they have failed in agreement on common values for coefficients. The coefficients for water at the same temperature in their research are varied over more than three orders of magnitudes.

Therefore, the coefficients should be determined based on parametric study on target problem. Excessively large values lead to numerical stiffness problems, while values that are too small result in an over-diffused metastable state region.

2.7.3 Difference between phase-changing models and homogeneous nucleation

The generation of liquid from vapor is usually referred to as a stochastic process. If the local pressure exceeds the saturation pressure, microscopic appearance/decay of liquid nuclei continuously occurs in the vapor phase. This fluctuation is amplified when the local pressure achieves a certain level of supersaturation and the liquid nuclei can readily maintain its phase. This process is taken into account in the nucleation model with the exponential term in Eq. (2.101). With the exponential term, the condensation process of the nucleation model is abruptly triggered only when the local pressure exceeds a certain level of supersaturation. Thus, there exists some distance lagging between the location of observable condensation and the region where the local pressure reaches the saturation pressure. On the other hand, the Hertz-Knudsen equation-based model immediately starts the condensation process if the local pressure is greater than the saturation pressure. From this point of view, the Hertz-Knudsen equation-based model may fail to capture the local physics unless flow fields expands suddenly (or the saturation pressure drops rapidly) so that the distance lagging effect can be ignored.

2.8 Adaptive mesh refinement technique

In the early stages of adaptive mesh refinement technique on structured grid, Berger *et al.* [38–40] suggested patch-based AMR technique which introduce the local refined patch around the region requiring more detailed resolution as Fig. [7b]. He extended applicable target problem from parabolic PDE to hyperbolic PDE, 2-D euler equation and 2-D Navier-Stokes equation.

Although patch-based AMR technique has been shown to be successful on many applications, it should obtain solutions on all levels to update flow properties on finest grid. Furthermore, it is often pointed out that refined grid could cover the unnecessary regions.

Block-based AMR technique, which is shown in Fig.[7c], predefines the local blocks to make nested fine grid. It then refines all cells in block if refining target cell is included. Therefore, it can be easily implemented and have a positive aspect in constructing tree data structure to track the neighboring and parent cells. However, it is also readily cover the unnecessary cells for refinement, and thus user's pre-definition on local block determines overall computational efficiency and parallel scalability. Recently, many researches have been conducted to overcome the efficiency and scalability problem

in block-based AMR technique such as Quirk [41], Berger [42], and Groth *et al.* [43].

Cell-based AMR technique refines the grid individually according to solution as Fig. (7d). It can avoid refining unnecessary cells, and hence have a benefit on computational efficiency and flexibility on target problems. However, it should keep the cell connectivity data on every cells, and thus requires substantial computer memory.

Among the listed types of AMR technique, cell-based AMR is employed in this research because the flow field in TVC is stationary, and thus does not need to update cell connectivity (edge database) data frequently. The computing algorithm with and without AMR techniuq is shown in Fig. (8).

Before starting the iteration process to acquire the converged solution, edge database, which contains informations on consisting node and neighboring cell for each edges, should be build up. At the same time, informations on consisting edges for each cells are also stored.(Fig. (9a)) In iterative computations, the cells, which should be refined, are flagged based on threshold value. Then additional nodes to divide edges and center of cell are added on node information.(Fig. (9b)) The pre-existed edges are then deleted and new edges are added on edge database. In this stage, neighboring cell indexes on each

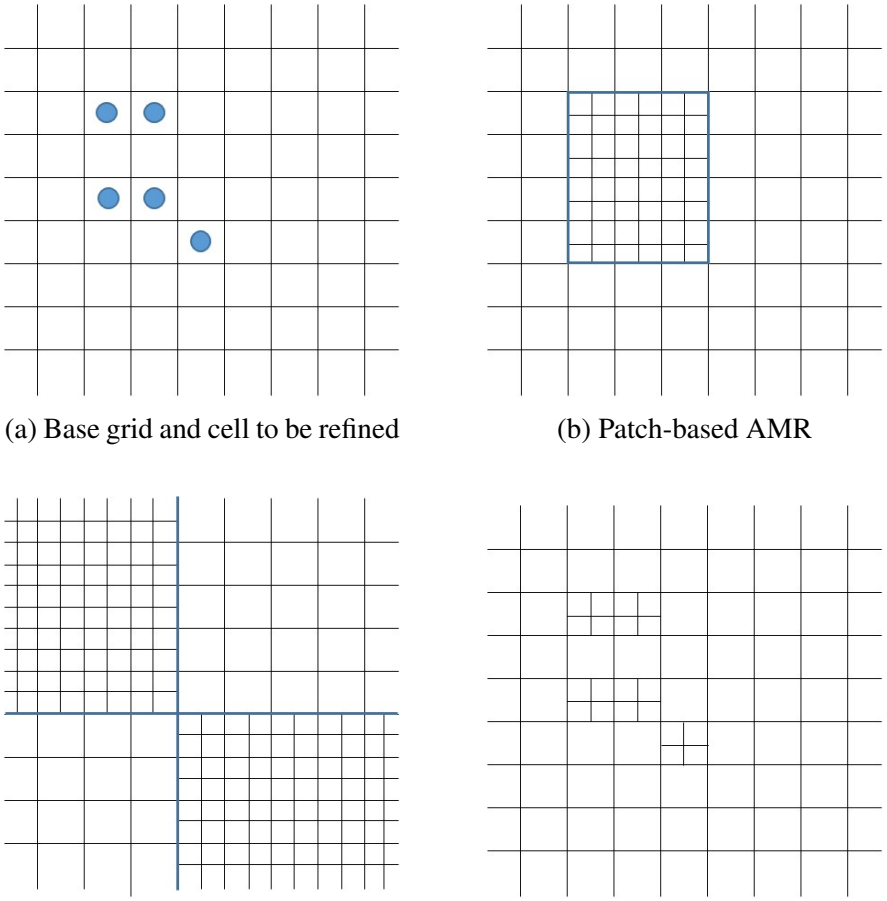

(a) Base grid and cell to be refined

(b) Patch-based AMR

(c) Block-based AMR

(d) Cell-based AMR

Figure 7: Types of adaptive mesh refinement technique

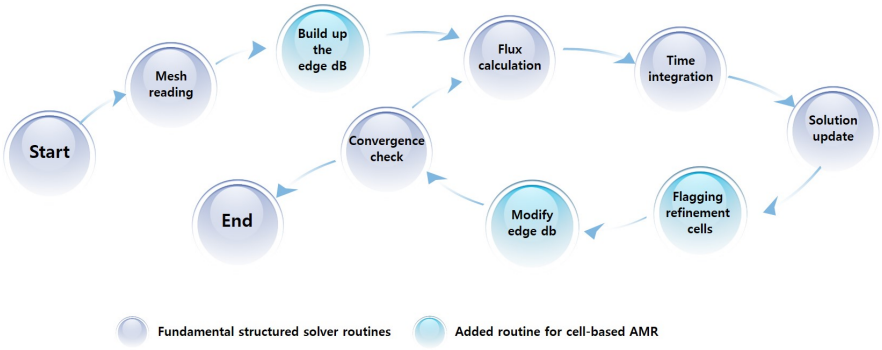

Figure 8: Fundamental structured solver routines and added routines for AMR

edges are also added.(Fig. (9c)) Finally, informations on consisting edges for each cells are modified.(Fig. (9d))

Fig. (10) shows base grid, resultant grid after 3-stage AMR and corresponding pressure contour on transonic NACA0012 problem. Comparing pressure contour in Fig. (10a) and Fig. (10b), AMR technique can desribe more shape pressure jump after shock, and it can be observed again in Cp curve shown in Fig. (10c). With AMR technique, resolution of shock is improved as the level of finer grid, which increases the number of grid for 4 times. However, the grid clustering level is concentrated on important region such as shock, and hence its computing efficiency is much higher as table 7.

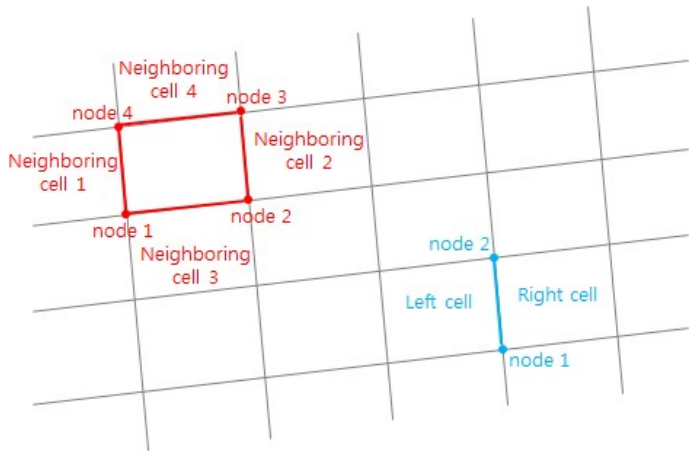

(a) Build up the edge database and cell informations

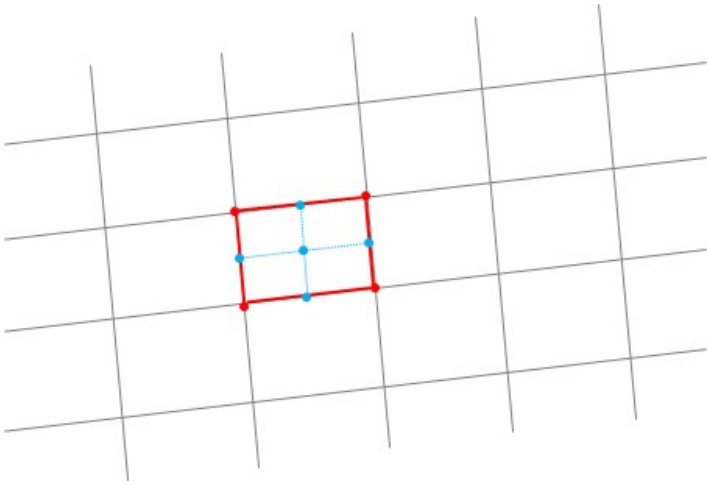

(b) Flagging the refining target cell and add the new nodes

	Base grid	AMR grid	Finer grid
Number of cells	128×128	128×128 + 4012×4	256×256
Elapsed time(sec)	308	1154	4980

Table 7: Comparison between base grid, AMR, and fine grid for number of cells and elapsed time

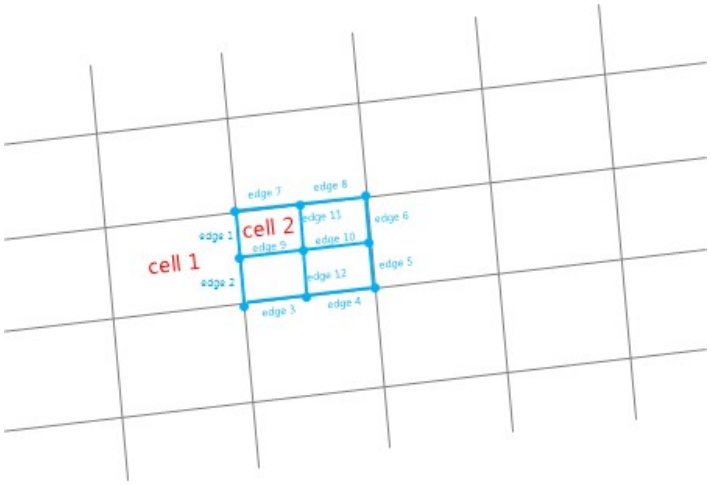

(c) Build up the new edge database

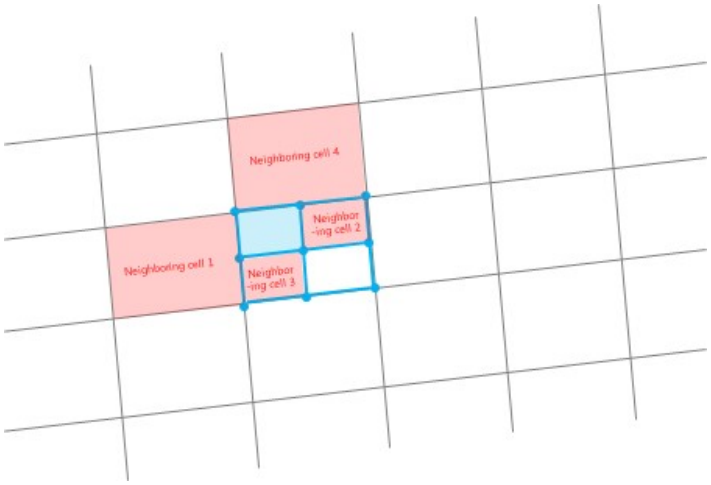

(d) Modify the cell informations

Figure 9: Modifying process for edge database in AMR process

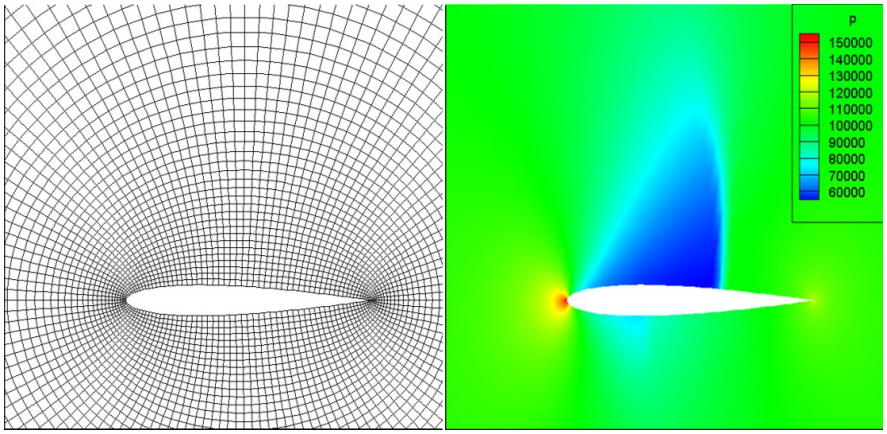

(a) Base grid and pressure contour

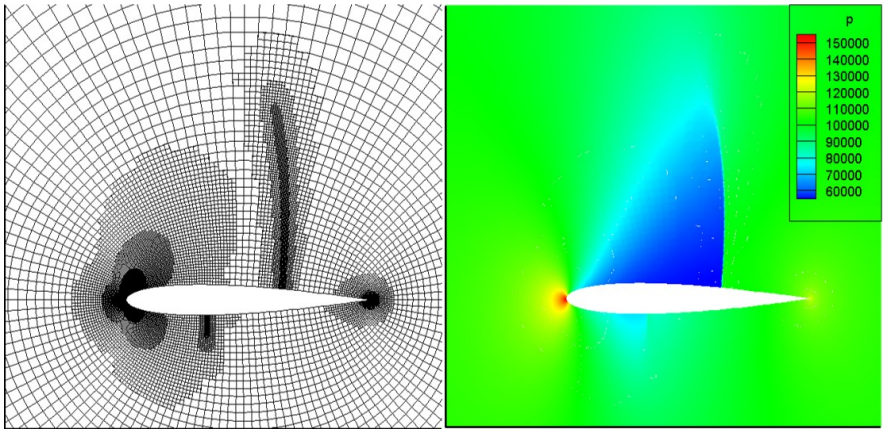

(b) 3-stage AMR grid and pressure contour

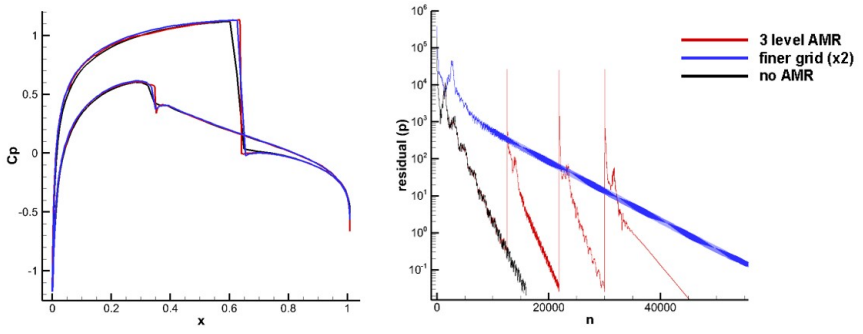

(c) Comparison between Cp curves and convergence history

Figure 10: Comparison between base grid and AMR results on transonic NACA0012 problem

2.9 Higher order interpolation

Monotone Upstream-centered Schemes for Conservation Laws (MUSCL) has been widely used to archieve higher accuracy even if the target flow field contains discontinuity such as shock. It is developed based on one-dimensional analysis, and expanded on two- and three-dimensional computations with dimensional splitting approaches. Therefore, MUSCL is reported to be insufficient or almost impossible to control oscillation near shock discontinuity in multiple dimension [44].

Recently, multi-dimensional limiting process (MLP) has been suggested as a solution for this problem. It is developed based on observation that the dimensional splitting approach can not consider any informations on distribution of properties ar cell vertex, whose information becomes important if property gradient is not aligned with local grid lines. The properties on vertex point is expressed in terms of variations across the cell-interface, and then properties on cell-interface are determined satisfying multi-dimensional limiting condi-

tion using restriction coefficient α as follows:

$$\bar{q}_L = \bar{q}_{i,j,k} + 0.5\phi\left(r_L^{\xi}, \alpha_L, \beta_L\right) \triangle q_{i-1/2,j,k}$$
$$\bar{q}_R = \bar{q}_{i,j,k} - 0.5\phi\left(r_R^{\xi}, \alpha_R, \beta_R\right) \triangle q_{i+3/2,j,k} \tag{2.123}$$

In Eq. (2.123), β is the local slope evaluated by a higher order interpolation. The restriction coefficient α, for example, along the ξ-direction is evaluated if $\triangle q_{\xi}^{p} \geq 0$,

$$\alpha_L = g\left(\frac{2max\left(1, r_L^{\xi}\right)\left(\bar{q}_{p,q,r}^{max} - \bar{q}_{i,j,k}\right)}{\left(1 + \frac{\triangle q_{\eta}^{q}}{\triangle q_{\xi}^{p}} + \frac{\triangle q_{\zeta}^{r}}{\triangle q_{\xi}^{q}}\right)_{i,j,k} \triangle q_{i+1/2,j,k}}\right)$$
$$\alpha_R = g\left(\frac{2max\left(1, r_R^{\xi}\right)\left(\bar{q}_{p,q,r}^{max} - \bar{q}_{i,j,k}\right)}{\left(1 + \frac{\triangle q_{\eta}^{q}}{\triangle q_{\xi}^{p}} + \frac{\triangle q_{\zeta}^{r}}{\triangle q_{\xi}^{q}}\right)_{i+1,j,k} \triangle q_{i+3/2,j,k}}\right) \tag{2.124}$$

where $r_L^{\xi} = \frac{\triangle q_{i+1/2,j,k}}{\triangle q_{i-1/2,j,k}}$, $r_R^{\xi} = \frac{\triangle q_{i+1/2,j,k}}{\triangle q_{i+3/2,j,k}}$ and $g(x) = max(1, min(2, x))$. The coefficients α for other directions can be calculated in simillar way. If β can be computed with third order polynomial or fifth order polynomial, and it is called MLP3 or MLP5, respectively. More detailed informations can be found at Ref. [44, 45].

Chapter 3

Numerical results

3.1 Numerical validations

3.1.1 Flow inside an ejector-nozzle

Before examining the phase-changing flows, the shock-resolving capability of the present numerical solver is validated using an ejector-nozzle problem. This problem was experimentally investigated by Gilbert *et al.* [46] and numerically validated by Georgiadis *et al.* [47]. Even though the working fluid is not steam but a perfect gas, underlying flow physics is similar to that of the TVC system. It contains the entrainment effect along with the shock-train, turbulent mixing, and the interaction between the expansion fan and shear layer. Table 8 summarizes the flow conditions.

Figures 11 and 12 show the Mach-number contour and velocity profiles compared at specific positions on the downstream side of the

	Pressure(Pa)	Temperature(T)
Primary inlet	246348.8(total)	357.78(total)
Suction inlet	101559.4(total)	305.56(total)
Discharge outlet	92734.2(static)	-

Table 8: Boundary conditions for ejector-nozzle problem

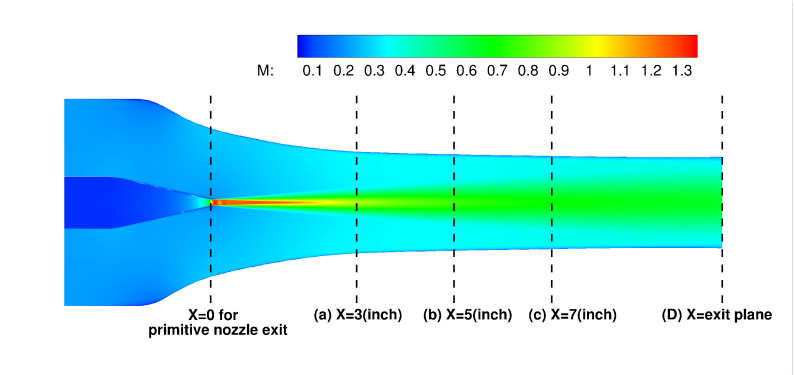

Figure 11: Mach number distribution

nozzle exit. The computed results yield quite a reasonable agreement with the experimental data of Gilbert *et al.* and the numerical results by the WIND code.

3.1.2 Condensing flows in a nozzle

The cases of experiments conducted by Moses *et al.* [10] and Moore *et al.* [11] are numerically validated with two phase-changing models. The flow fields is assumed to be symmetric with respect to

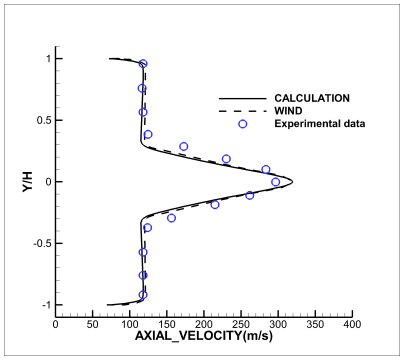

(a) $x = 3.0(inch)$

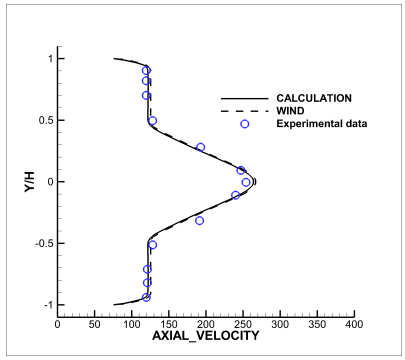

(b) $x = 5.0(inch)$

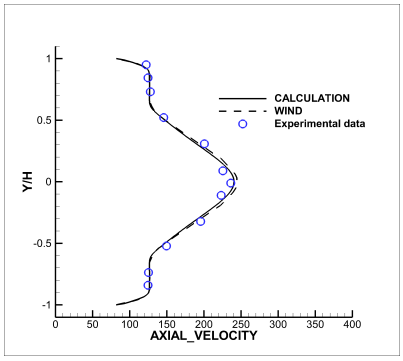

(c) $x = 7.0(inch)$

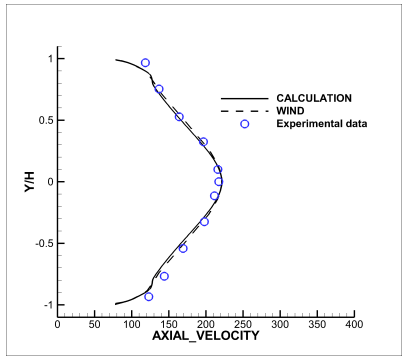

(d) $x =$ exit plane

Figure 12: Comparison of velocity profiles

the nozzle centerline, and the computational domains are shown in Fig. 13. The boundary condition at the inlet is specified using the total pressure and total temperature as summarized in Table 9, and the supersonic outlet boundary condition is imposed.

As shown in Fig. 14, computations using the nucleation model are in good agreement with the experimental data, while the Hertz-Knudsen equation-based model yields somewhat noticeable differ-

(a) Geometry of Moses *et al.*

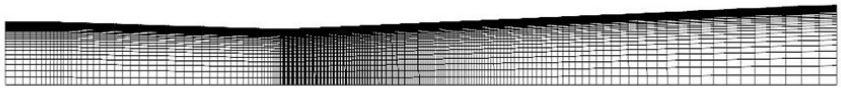

(b) Geometry of Moore *et al.*

Figure 13: Geometries for numerical validation

	Total pressure	Total temperature
Moore B	25000(Pa)	357.6(K)
Moore C	25000(Pa)	358.6(K)
Moses and Stein	70727.52(Pa)	377.15(K)

Table 9: Inlet boundary conditions

ences. The reason for such discrepancy is associated with the phase-changing process described by each model.

The flow is accelerated as it passes through the convergent part of the nozzle, reaching the sonic condition near the throat. Then, weak expansion is developed to further lower the local pressure, temperature and saturation pressure on the divergent part. At this point,

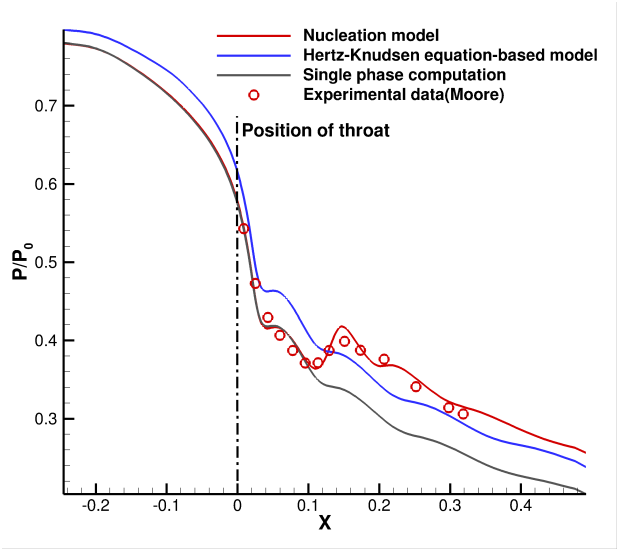

(a) Moore B

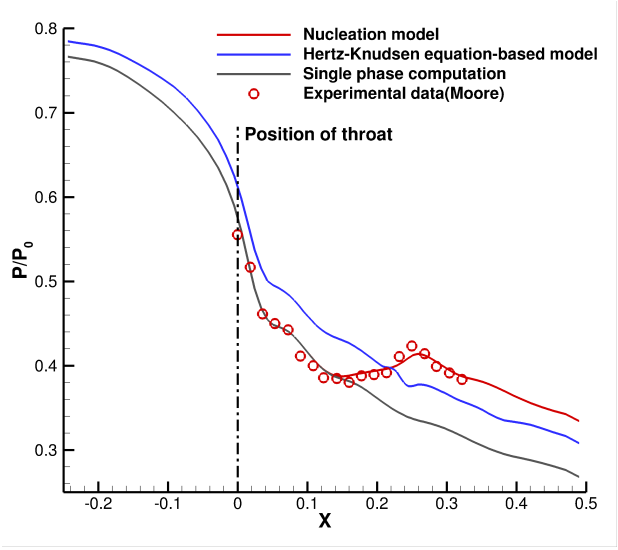

(b) Moore C

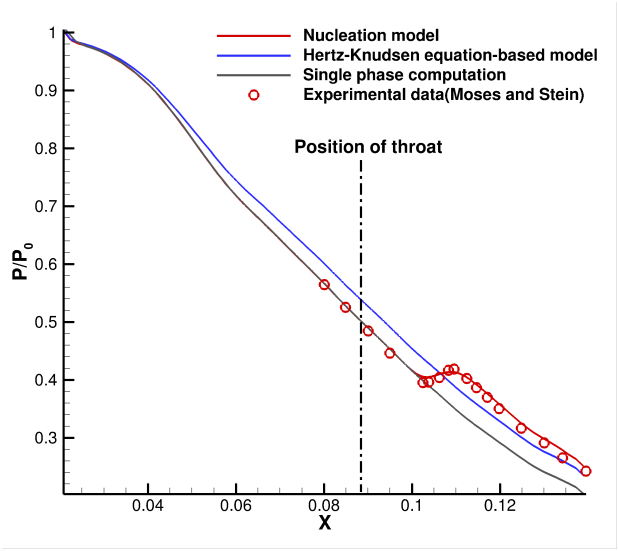

(c) Moses and stein

Figure 14: Comparison of pressure distributions along the centerline

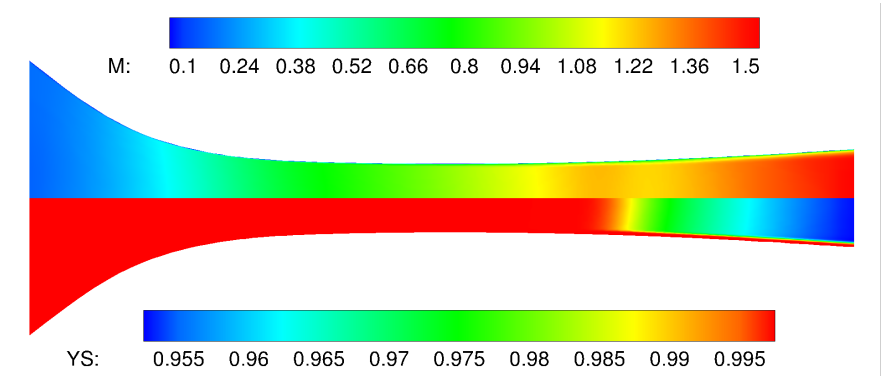

Figure 15: Mach-number and mass-fraction contours for Moses and Stein nozzle

the Hertz-Knudsen equation-based model starts to generate the liquid phase immediately after the throat, and the divergent part induces further expansion. The liquid phase is thus continuously generated. On the contrary, the nucleation model does not generate the liquid phase right after the nozzle throat but expands the gas further while maintaining a supersonic flow condition. Hence, the pressure distributions by the nucleation model and single-phase computation are almost identical up to the starting position of nucleation. When a certain level of supersaturation is achieved after the starting position, the nucleation rate is rapidly increased and the liquid phase is developed. As a result, substantial latent heat is released into the flow fields during the phase-changing process, leading to the rise of the local pressure. Yang *et al.* [48] referred to the sudden pressure rise due to the phase change as a condensation shock. As seen in Fig. 15, however, the condensation shock is not strong enough to produce a subsonic downstream condition as typically observed in an aerodynamic shock.

Figure 16a illustrates the overall phange-changing process in terms of pressure. It is observed that the local pressure by the nucleation model suddenly increases in the diverging part due to the condensation shock, whereas the one by the Hertz-Knudsen equation-

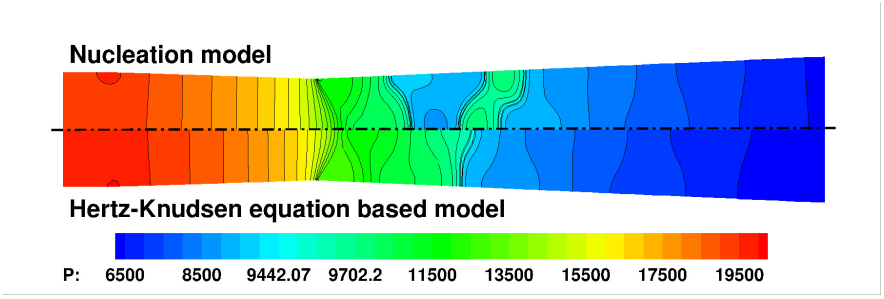

(a) Pressure contour

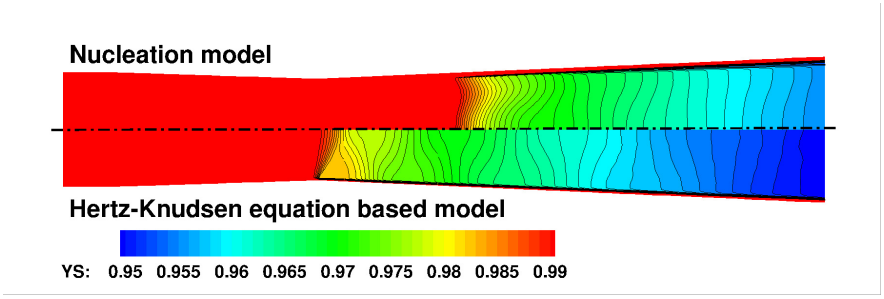

(b) Mass fraction contour

Figure 16: Comparison between two phase-changing models for Moore B

based model is monotonically decreasing. Figure 16b compares the mass fraction contour between the two phase-changing models, clearly indicating that the Hertz-Knudsen equation-based model yields continuous alteration from the gas to the liquid phase after the nozzle throat, while the phase change by the nucleation model starts after the sudden increase in the local pressure.

3.2 Flow field inside TVC

In this section, numerical results for the flow fields around the TVC using single- and two-phase computations will be presented. For the purpose of objective comparison, single-phase computations are evaluated using ANSYS FLUENT under the ideal gas condition for steam, and two-phase computations are carried out with the in-house code based on the numerical methods stipulated in Chapter 2.

The suction performance data of target TVCs are experimentally measured by Doosan Heavy Industries, and it will be normalized with the experimental data due to company's security problem. The operating conditions for each TVCs are varied from 2.5(bar) to 15(bar).

The fundamental flow physics in TVC are firstly addressed, and then operational modes of TVC are then reproduced to confirm the consistency of present computations. Then examining the three-dimensional effect on flow field inside TVC is followed. The grid dependency is minimized in our computations using cell-based AMR technique, and its influence will be continuously addressed.

Figure 17 shows an example of three-dimensional modeling for target TVC. The total pressure boundary condition is imposed on both the primary and suction nozzle inlets, while the static pressure condi-

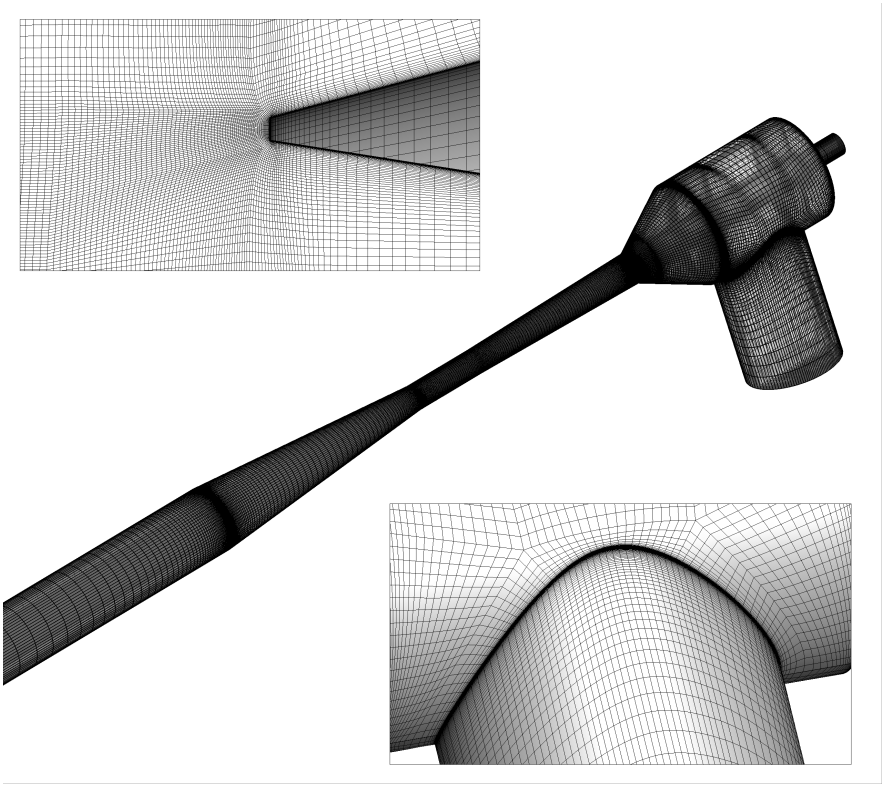

Figure 17: Perspective view of three-dimensional modeling, detailed view around junction part for main nozzle and suction nozzle and primary nozzle exit

tion is applied to the discharge outlet.

Based on computed results with single- and two-computations, the necessity of multi-phase modeling for flow field in TVC will be further emphasized. Finally, comparison between two-phase modelings in this research will be presented.

3.2.1 Flow physics in Thermal Vapor Compressor

The main role of TVC is entraining and re-pressurizing the suction steam, whose temperature and pressure are decreased in desalination process, by ejecting the primary steam, whose temperature and pressure are substantially higher then suction steam. When primary steam is ejected from primary nozzle exit, velocity difference between developed supersonic core flow and stationary surroundings generates shear mixing layer. At the same time, continuous expansion in diverging part of primary nozzle exit generates oblique shock. The shock is reflected as a expansion fan when it approaches to shear layer. Because expansion fan increases local velocity, strain rate around shear layer and corresponding turbulent kinetic energy is increased. The generated each expansion lays are reflected as a weak compression waves again when it approaches to shear layer, and they are merges into secondary oblique shock. The overall flow physics addressed above are shown in Fig. 18.

Figure 19 shows the entrainment ratio curve, centerline-pressure distributions, and corresponding Mach-number contours obtained by two-phase computations for configuration 4. Generally, the TVC is operated in the double-choked mode, where the throats of both the

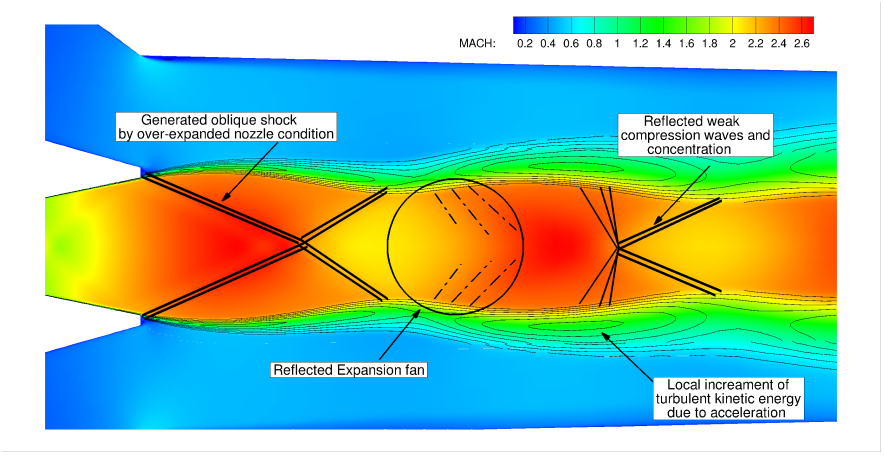

Figure 18: Flow structure in Thermal Vapor Compressor

primary and main nozzle are choked. In this mode, the entrainment ratio remains constant even when the back pressure is increased, and optimal suction performance is achieved. This behavior is maintained until the critical back pressure is reached. When the back pressure is greater than the critical back pressure, the throat of the main nozzle deviates from the choked condition and the entrainment ratio as well as the mass flow rate in the suction nozzle starts to decrease. The operating condition is then turned into the single-choked mode. If the back pressure further increases, the TVC loses its capability to entrain steam and reverse flow is developed in the suction nozzle.

Examining the Mach-number contours in the double-choked mode, Fig. 19c for the conditions A and B of Fig. 19a, it can be observed

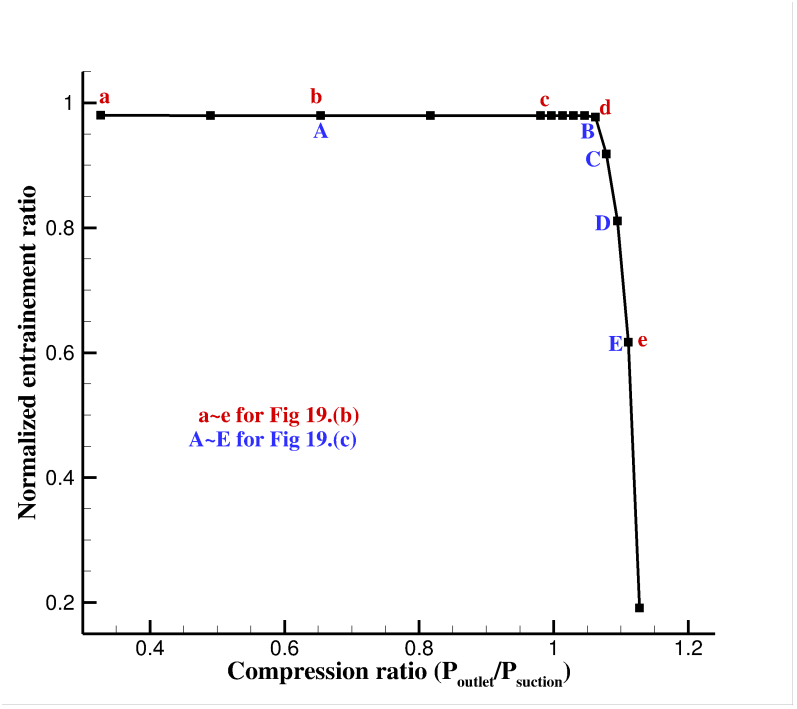

(a) Entrainment ratio curve

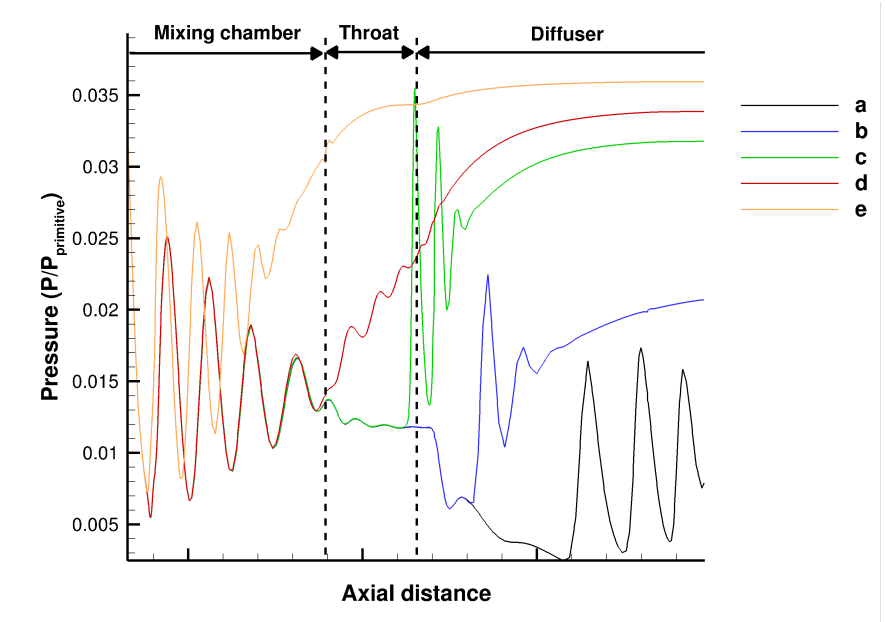

(b) Centerline pressure distribution for configuration 4

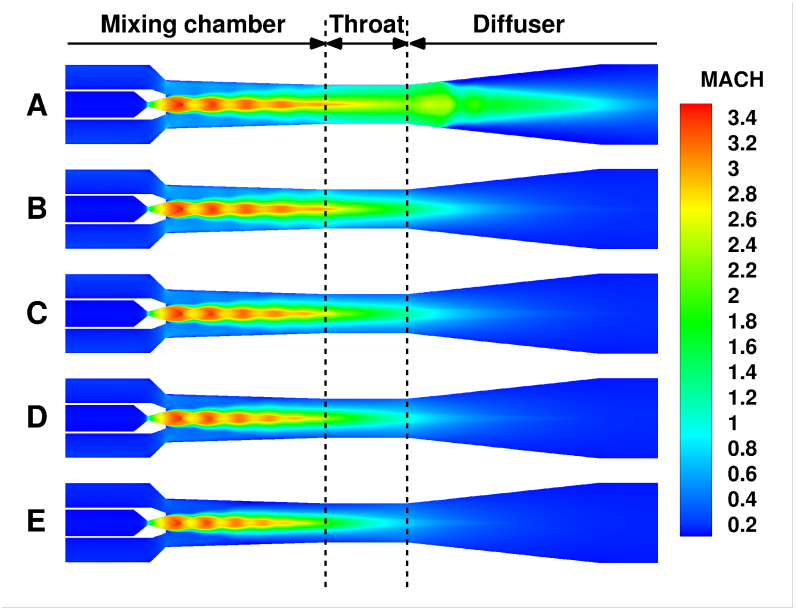

(c) Mach number contours

Figure 19: Suction performance and Mach-number contours under various backpressure

that the shock-train region of the supersonic core flow in the mixing chamber is similar with each other, while the terminal shock position is retreated as the discharge outlet pressure increases. If the discharge outlet pressure further increases, the operation mode changes into the single-choked mode and the shock-train region in the mixing chamber begins to shrink as shown in the conditions B $\sim$ E in Fig. 19c.

This transition can be clearly seen in Fig. 19b, which compares the pressure distributions along the centerline. Conditions from $a \sim c$ belong to the double-choked mode, while conditions d and e represent the critical condition and the single-choked mode, respectively. The secondary oblique shock in the diffuser moves toward the upstream side as the back pressure increases from the condition a to c, but the pressure fluctuation across the shock-train region in the mixing chamber remains unchanged. The secondary oblique shock is then fully merged into the shock-train region when the back pressure increases beyond the critical point d. Further increase in the back pressure causes the shrinking of the shock-train region.

It was observed that the length of the shock-train region and the entrainment performance are closely related to the effective area [49]. Huang *et al.* reported that there exists a passage, located near the throat region, which induces the choked condition for the suction

stream. Even with computational visualization, its exact location is difficult to pinpoint. However, it is clear that the effective area would change when the secondary oblique shock is merged into the shock-train in the mixing chamber. Thus, local mesh refinement is introduced to accurately capture the shock-train region which is crucial to the accurate prediction of the TVC performance.

3.2.2 Three-dimensional effects

The suction nozzle in experiments conducted by Doosan Heavy Industries is combined with main nozzle in vertical direction as Fig. 17. Therefore, the flow field inside TVC in experiments would not be axi-symmetrically formed. The axi-symmetric assumption, however, can save computational time by reducing dimension of solver, and makes grid generation process easily. Therefore, three-dimensional effect on computed suction performance is examined by varying junction part modeling as Fig. 20.

The computed entrainment ratios are shown to be almost independent on modeling for junction part of suction nozzle. The axi-symmetric modeling and real configuration modeling on TVC operating about 6(bar), for example, estimated entrainment ratio as 0.65 and 0.66, respectively. The main reason for this result is arising from

choking condition, which is emphasized in previous section.

The suction stream entrained from vertically combined suction nozzle makes unsymmetrical flow structure as Fig. 21. Even though tiny reversed flow region is observed near the diffusing part of main nozzle, its effect on choking condition is enough to be negligible. The estimated pressures at the wall with 2-D axisymmetric assumption, 3-D axisymmetric modeling and real configuration modeling are thus similar to each other as Fig. 22. Therefore, 2-D axisymmetric assumption is utilized in computations in following sections.

3.2.3 Grid dependence and AMR technique

As mentioned previously, the level of the grid density in the shock-train region is important because the length of the shock-train determines whether the TVC operates in the single- or double-choked mode. A cell-by-cell adaptive mesh refinement technique was employed to minimize the grid dependency of the computed results. A pressure gradient with a supersonic flow condition was chosen as the refinement criterion to restrict the grid refinement to the shock-train and shear layer.

Figure 23a represents an example of the convergence history with a coarse mesh (33,000 cells) and the solution enhancement by

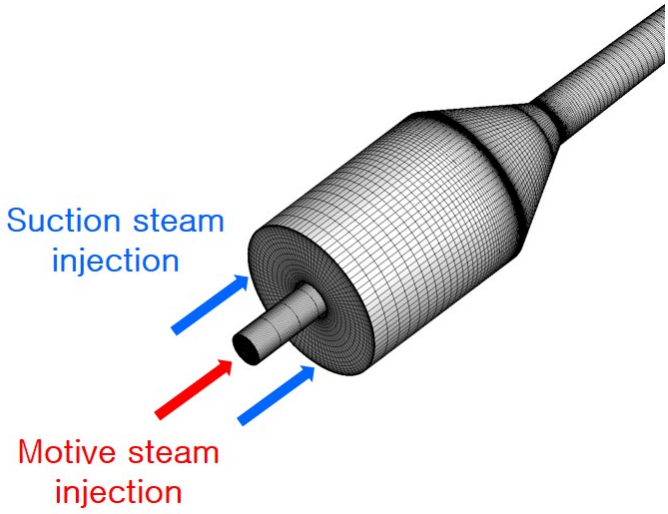

(a) 3-D axi-symmetric modeling, E.R=0.66

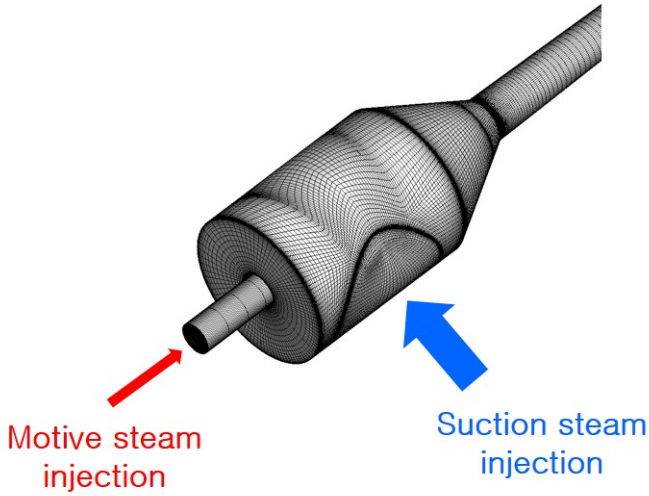

(b) 3-D real configuration modeling, E.R=0.65

Figure 20: Junction modeling and computed entrainment ratio

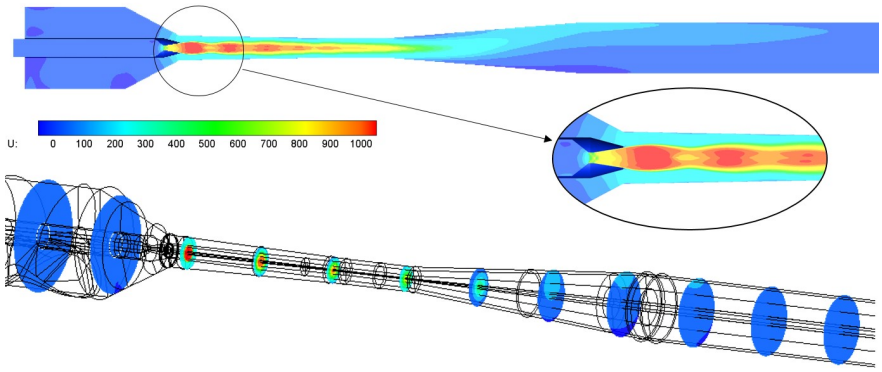

Figure 21: Unsymmetric flow structure in real configuration modeling

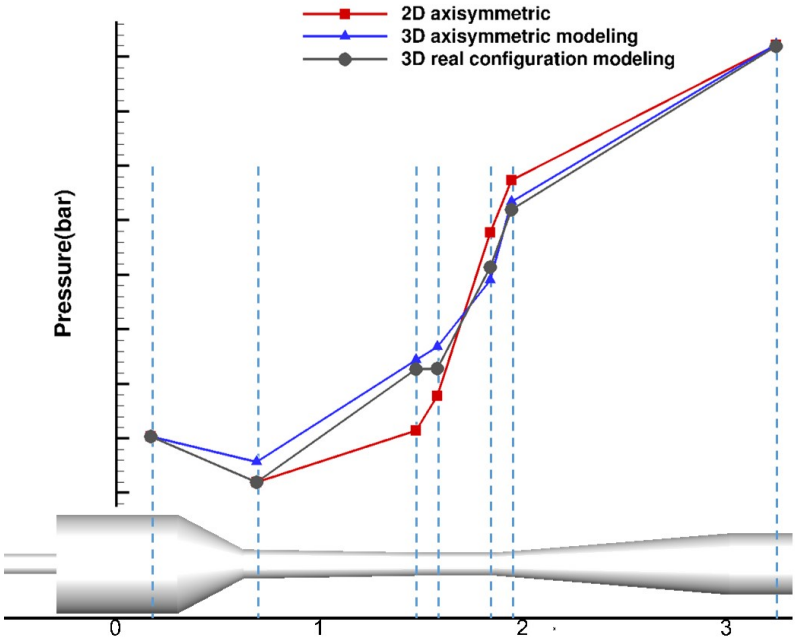

Figure 22: Comparison of computed wall pressure between junction modelings

applying the 3-level AMR refinement (54,000 cells) for configuration 1. Compared with the experimental data, the coarse mesh grossly underestimates the entrainment ratio by 45%, but the AMR technique improves it by reducing the error to 3%. Figure 23b shows the resultant mesh after AMR, by which the grid is properly clustered around the shock-train and shear layer.

Computing the TVC flow fields with a coarse mesh could yield a disastrous result because numerical dissipation depending on grid size excessively smears physical properties around the shock-train region. Under-resolved shear layer would cause not only inaccurate momentum transfer from the supersonic core flow to the suction stream but also the shock-train region to be overly diffused by excessive numerical viscosity. Figure 24 demonstrates that the effective length of the shock-train is evidently shortened because of excessive numerical dissipation and overestimation of turbulent properties. Thus, all computations in the following sections are performed using the AMR technique.

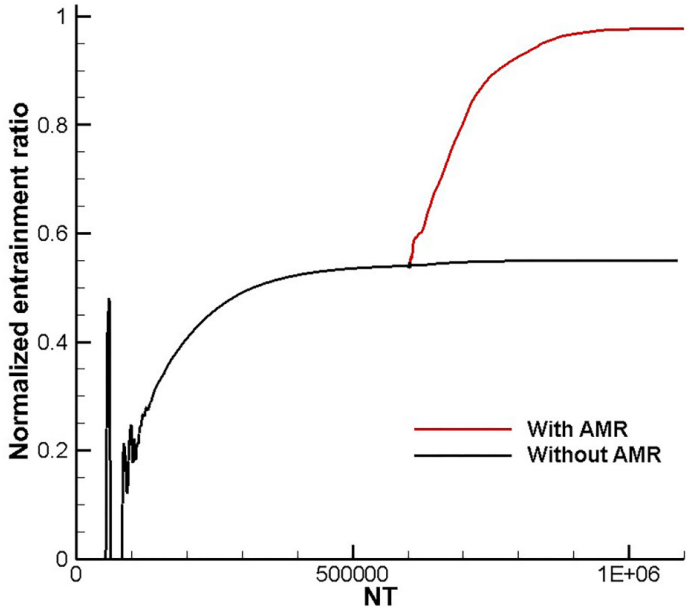

(a)

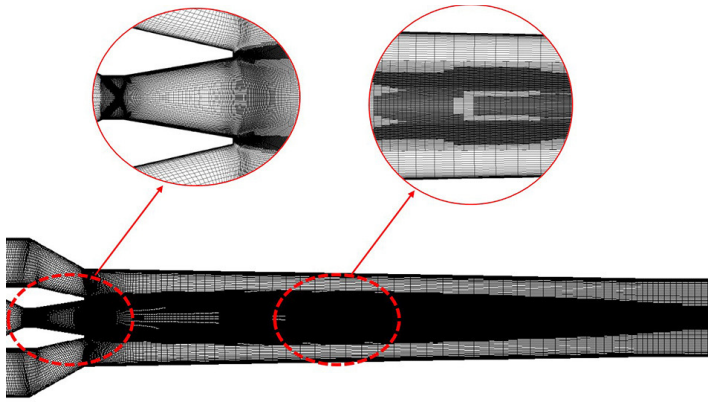

(b)

Figure 23: Convergence history (a) and resultant mesh after AMR (b)

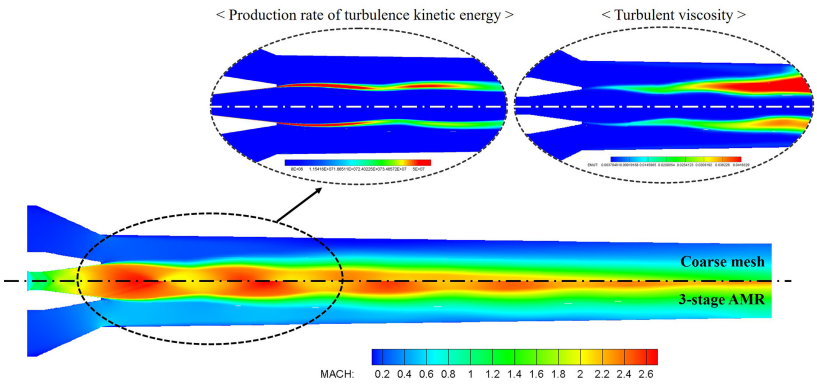

Figure 24: Comparison of Mach-number and turbulent properties between coarse mesh and AMR results

3.2.4 Phase-changing phenomena and entrainment performance

The entrainment performance of the TVC using single-phase computations with an ideal gas assumption is compared with that of two-phase computations. It is well-known that the ideal-gas assumption is a reasonable choice to obtain acceptable computed predictions in many cases [1–3]. As shown in Table 10, however, it may yield substantially incorrect results under several configurations and/or operating conditions. On the contrary, computations with the two-phase models improve the predicted suction performance significantly. In particular, the results for configurations 1, 2, and 5, which are subject to huge errors under single-phase computations, match the experi-

mental data very well in two-phase computations.

The continuous flow expansion in the diffusing part of the primary nozzle alters a certain amount of the thermodynamic energy into the kinetic energy. Some portion of this converted energy is actually consumed in the condensation processes which is taken into account for two-phase computations but not in single-phase computations. This mechanism also happens when the flow passes through expansion fan. Therefore, the temperature or pressure decrement as well as the strength of expansion fan is weaker in two-phase computations. Similarly, some portion of the converted energy across the shock (the kinetic energy to the thermodynamic energy) is used in the evaporation process, and thus the shock strength is generally weaker in two-phase computations.

Figure 25, which compares single- and two-phase computations for configuration 2, confirms the above observation by showing more intense variation in Mach-number and pressure distribution for single-phase computation. Due to the absence of the phase-changing process in the primary nozzle, the Mach-number after the primary nozzle exit reaches a much higher value in single-phase computation. As a result, the strength of the shock-train is stronger and shows the vigorous pressure fluctuation, as seen in Fig. 25b.

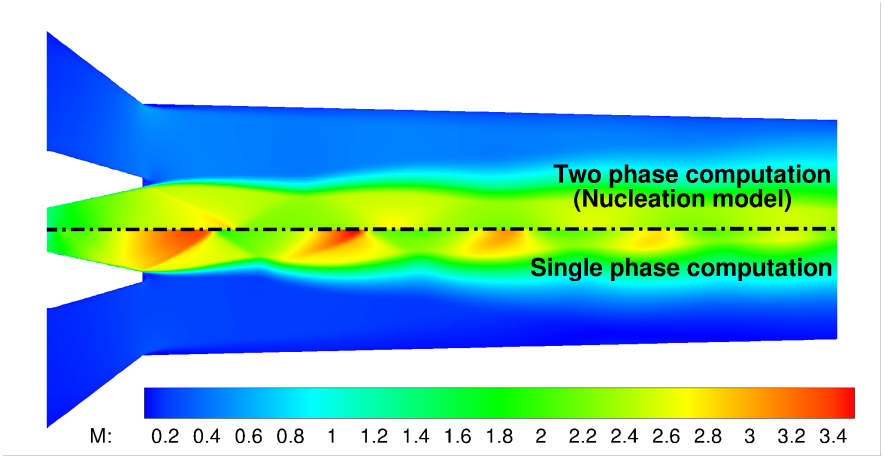

(a) Mach-number contours

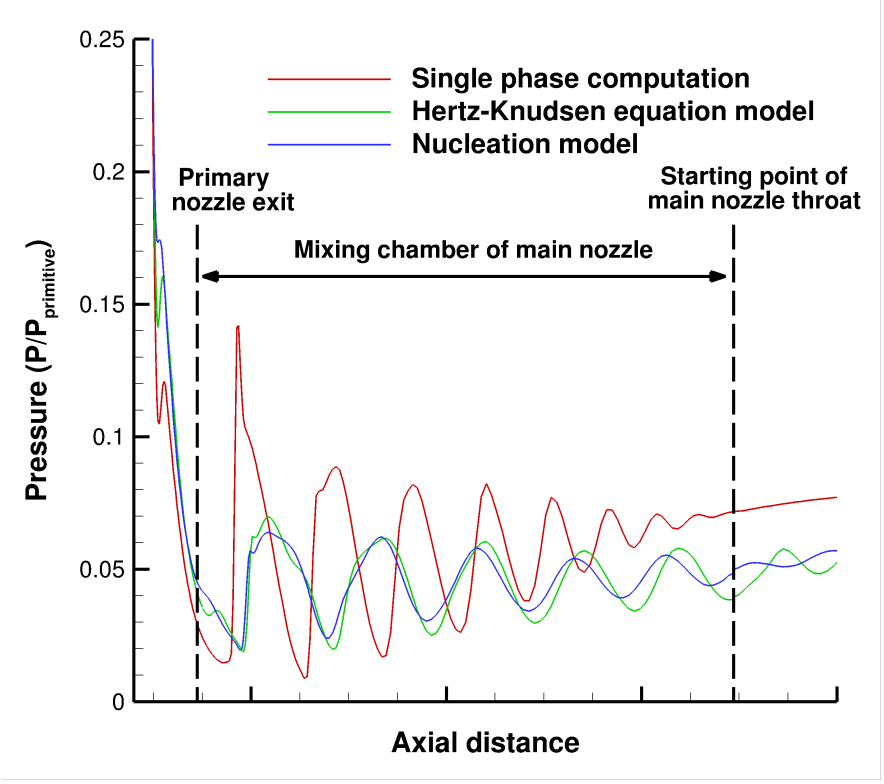

(b) Pressure along to the centerline

Figure 25: Comparison between single- and two-phase computations for configuration 2

When examine the temperature distribution, computing the steam-flow field with single-phase assumption may yield totally erroneous results in the physical sense. Figure 26 compares the temperature distribution between single- and two-phase computations. Temperature decreases in both single- and two-phase computations due to the flow expansion in the primary nozzle, but it should be greater than the triple point of water (273.15K). Two-phase computation satisfies this physical constraint because condensation weakens the strength of expansion fan, as in Fig. 26b, while single-phase computation does not. Consequently, the shock-train region is totally unphysical under single-phase computation in the sense that its temperature is lower than the triple point temperature. The gray-marked area in Fig. 26a indicates the region lower the triple point temperature. Furthermore, the physically correct behavior of two-phase computation is also attributed to the difference in the heat capacity between the gas and liquid phases. The liquid phase generally has a larger heat capacity than the gas pahse, and thus it requires more heat to induce temperature variation.

The experimental conditions listed in Table 10 are near the critical back pressure which is the threshold pressure to divide the double-choked and single-choked modes. Thus, a small deviation from the

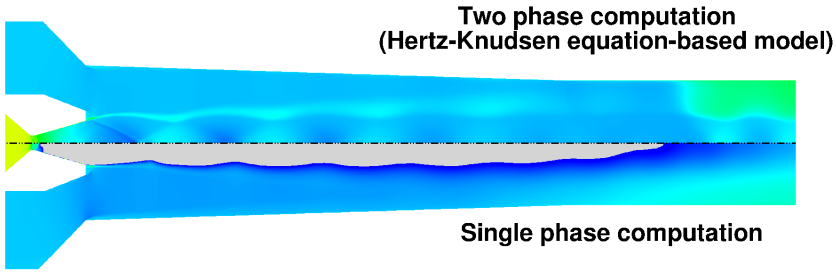

(a) Comparison of temperature contour

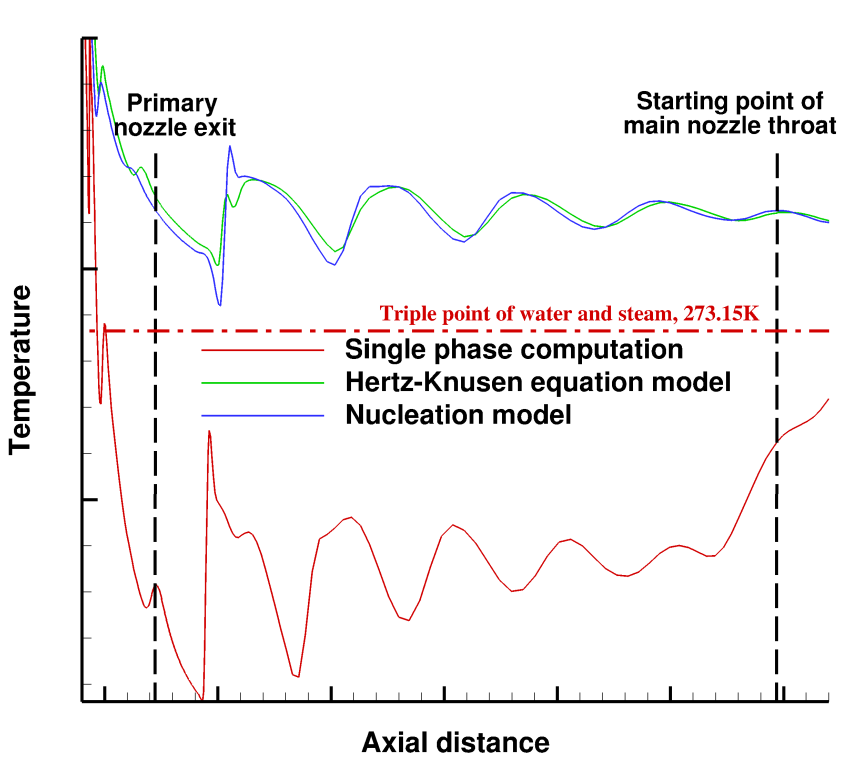

(b) Comparison of temperature distribution along to the centerline

Figure 26: Comparison between single and two phase computations

real physics may change the operational mode of the TVC. The flow conditions for configurations 1, 2, and 5 are the cases in which shortening the shock-train region caused by single-phase computations does alter the operational mode of the TVC from a double-choked mode to a single-choked mode. On the other hand, the entrainment ratio of the double-choked mode can be accurately predicted even with single-phase computations, if the discharge outlet pressure is sufficiently lower than the critical back pressure so that the shock-train sufficiently extends to the mixing chamber. Configurations 3 and 4 in single-phase computations are such cases. Even though single-phase computations do not capture the strength of the shock-train accurately, the TVC may be correctly operating in the double-choked mode.

Figure 27, which compares the Mach number distribution with sonic line, supports above statement. Because single-phase computation neglects the effect of latent heat in phase-changing phenomena, strength of compressible waves in shock-train region is substantially stronger than two-phase computation, and it thus results in faster deceleration of primary flow into the subsonic condition as Fig. 27a. As a result, single-phase computation predicts the TVC as if it is operating in single-choked mode, and hence it estimates the substantially

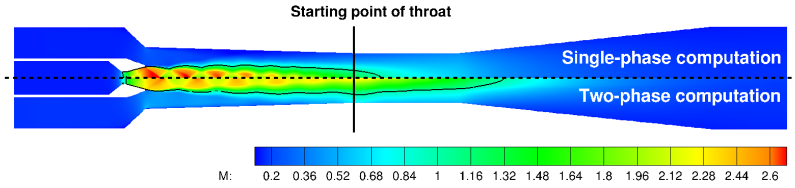

(a) Configuration 1

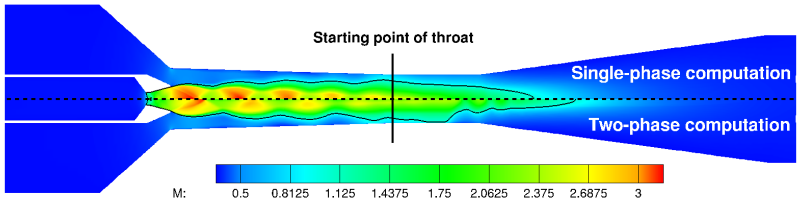

(b) Configuration 3

Figure 27: Mach number comparison between single- and two-phase computations

decreased suction performance.

On the other hand, there is adventitious cases which show the double-choked mode in single-phase computation even though it mis-predicts the strength of shock-train region as Fig. Mach number comparison for configuration 3, and it may be affected by sufficiently lower discharged outlet pressure than critical back pressure.

		Primary mass flow rate	Suction mass flow rate	E.R	E.R error
Config. 1	Single phase	1.017	0.538	0.529	47.1%
	Hertz-Knudsen	0.978	0.910	0.930	7.00%
	Nucleation	1.017	0.922	0.906	9.40%
Config. 2	Single phase	1.022	0.544	0.532	46.8%
	Hertz-Knudsen	0.985	0.958	0.972	2.76%
	Nucleation	0.995	0.973	0.978	2.15%
Config. 3	Single phase	0.931	0.974	1.047	4.67%
	Hertz-Knudsen	0.921	0.986	1.070	7.02%
	Nucleation	0.945	0.991	1.048	4.84%
Config. 4	Single phase	0.972	0.904	0.930	7.03%
	Hertz-Knudsen	0.954	0.934	0.980	2.02%
	Nucleation	0.975	0.942	0.967	3.34%
Config. 5	Single phase	0.995	0.379	0.381	61.9%
	Hertz-Knudsen	0.982	0.951	0.968	3.19%
	Nucleation	1.009	0.952	0.943	5.68%

Table 10: Comparison of entrainment performance with phase-changing models

3.2.5 Comparison of the phase-changing models

Table 10 indicates that two-phase computation models can predict the entrainment ratio to a reasonable degree of accuracy because they can properly capture the shock-train region in the mixing chamber by physically estimating its strength. Though additional experimental data such as the local pressure or temperature distirbution in the shock-train region might be necessary for more rigorous comparison, the centerline properties shown in Figs. 25b and 26b confirm that the performance of the two phase-changing models is more or less similar.

While the Hertz-Knudsen equation-based model shows somewhat unsatisfactory results for the validation problem (the condensed nozzle flow), the computed results for the TVC are quite satisfactory. It is associated with the operational conditions. The inlet pressure is moderately higher than the discharge outlet pressure in the validation problem, and the flow expands slowly. Consequently, the supersaturation level for condensation is not accomplished immediately after the throat, but delayed. For the flow fields inside the TVC, the pressure difference between the primary nozzle inlet and exit is high and sudden expansion is induced at the primary nozzle throat. The supersat-

uration level for condensation is then reached immediately after the throat. This leads to a similar exit pressure in both phase-changing models, even though the local flow physics inside the primary nozzle is different. Table 10 may suggest that the Hertz-Knudsen equation-based model is better than the nucleation model, but this is only in terms of the entrainment ratio. When comparing the mass flow rate (or the computed mass flow rate normalized by the experimental one), the nucleation model yields closer results to the experimental data which is attributed to the phase-changing process.

Figure 28 compares the two-phase models near the throat of the primary nozzle in terms of the mass fraction and density. The speed of sound in the liquid phase is generally much higher than that in gas phase, but in the mixture region, it rapidly drops to the order of the local flow velocity. The condensation process of the Hertz-Knudsen equation-based model occurs throughout the nozzle throat area, while it occurs only near the throat wall in the nucleation model, as shown in Fig. 28a. Both models predict that the local pressure exceeds the saturation pressure around the centerline of the nozzle throat, but the supersaturation for condensation is partially reached after the first expanding corner in the nucleation model. Due to such difference in the condensing region of the nozzle throat and the lowered mixture speed

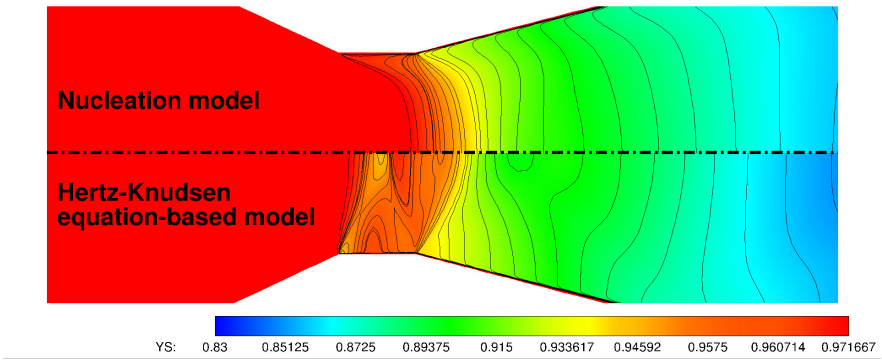

(a) Mass fraction

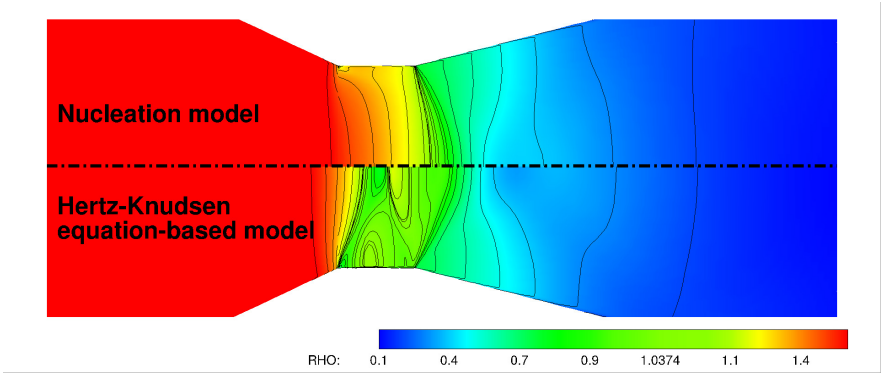

(b) Density

Figure 28: Comparison between phase-changing models near the primary nozzle throat

of sound, the behavior of the flow expansion is substantially different, as shown in Fig. 28b. While the density and mass flow rate are noticeably decreased in the Hertz-Knudsen equation-based model, the nucleation model does not yield such result because the supersaturation level is lower than that for condensation. Figure 25b shows that the first and second peaks of pressure fluctuation are similar be-

tween the two-phase models, but the decaying tendency of the shock-train region is relatively stronger in the nucleation model. As stated in Section 1, the shear layer plays a significant role in the momentum transfer from the supersonic primary flow to the suction steam as well as the decay of the shock-train region. Since the viscosity of the liquid phase is generally much higher than that of the gas phase, the liquid phase around the shear layer determines the length of the shock-train region. Figure 29 shows the droplet distribution (upper figure) and the generation rate (lower figure) in the nucleation model. It can be observed that the most pronounced region is near the wall, where the primary nozzle throat begins. As the generated droplets move on the downstream flow fields, the droplet number density is larger near the shear layer than the core flow of the shock-train region. In Eq. (2.116), the changing rate of the mass fraction due to the droplet growth is proportional to the number density. Thus, the liquid contents in the shear layer predicted by the nucleation model is larger and shaper than the other one as Fig. 30.

Detailed measuring data and/or experimental suction performance curves would be helpful to confirm the validity of each phase-changing model, but judging from the mass flow rate in the primary/suction nozzles and the entrainment ratio, the nucleation model provides more

accurate results. From the view point of computational cost, however, the Hertz-Knudsen equation-based model is advantageous because it can predict the suction performance with comparable accuracy without calculating the transport equation for the droplet number density.

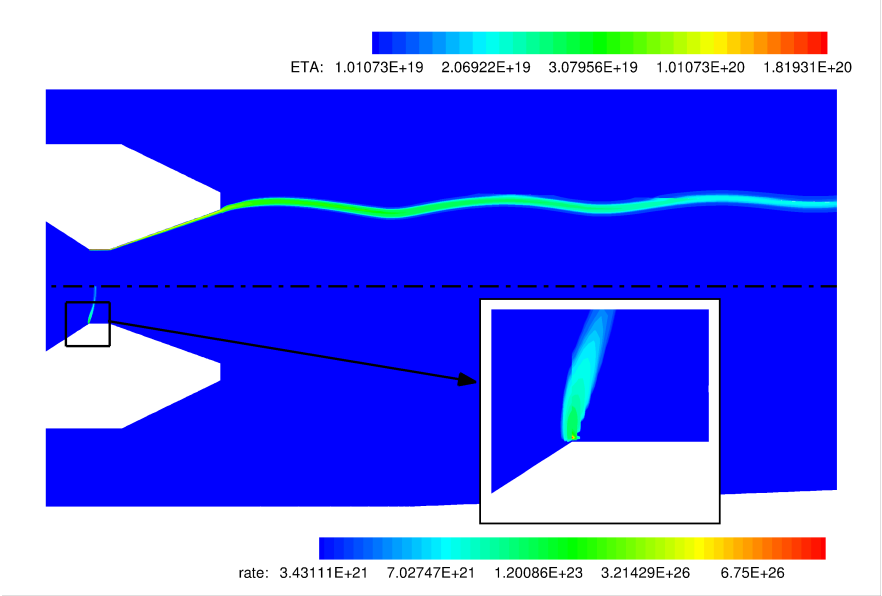

Figure 29: Rate of droplet generation in the nucleation model

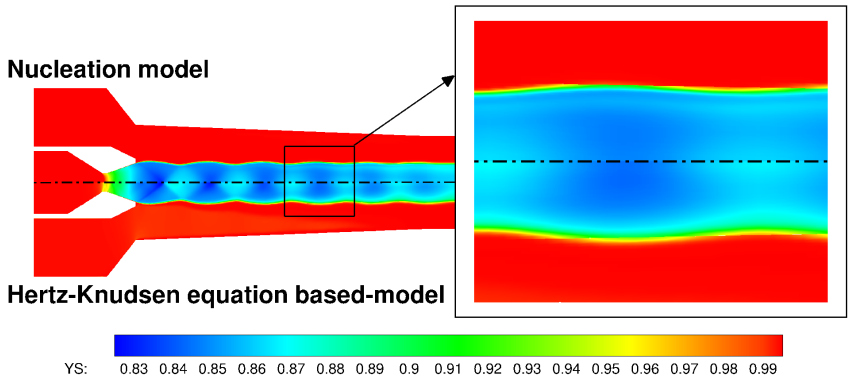

Figure 30: Comparison of mass-fraction contours

Chapter 4

Conclusion

4.1 Summary

The objective in this research is accurate estimation on suction performance of TVC, and it can not be accomplished without precise description on major flow physics, namely development of shock-train and shear mixing layer. There were many numerical researches to investigate the relation between suction performance and geometric parameter or operating pressure, however, most studies neglected phase-changing phenomena, and thus may fall into erroneous results on flow structure and corresponding computed suction performance. From this perspective, this research focuses on accurate prediction on flow physics including phase-changing phenomena while maintaining reasonable computational efficiency.

The multi-phase numerical framework is firstly built based on

homogeneous mixture model. The phase-changing process is considered with two distinct phase-changing models, Hertz-Knudsen equation-based model and nucleation model. Because flow properties should be accurately reflected for more reliable computed results, IAPWS-97 formulation is implemented as a equation of states, and its SBTL model is built for computational efficiency. The compressible flow physics is robustly captured with AUSMPW+_N scheme, and spatial accuracy is further enhanced with cell-based AMR technique.

Several experimental TVC models are then simulated with single-phase assumption and two-phase modelings. Computed results indicate that the major reason for mis-prediction in single-phase computation is associated with choking condition in primary and main nozzle throat. The TVCs are referred to be operating in double-choked mode if both primary and main nozzles are choked, while they are operated in single-choked mode if main nozzle is deviated from choking condition. Because the suction performance of TVCs is abruptly decreased in single-choked mode, predicting the flow physics related to choking condition, indeed shock-train region and shear mixing layer, is important for accurate and reliable computation.

Therefore, estimation on the strength of compressible waves and the length of shock-train region are arisen as a major factor which

should be computed accurately.

The kinetic and thermal energy of flow are exchanged each other according to position of shock or expansion fan. At this point, the effect of latent plays a major role determining the strength of these compressible waves in two-phase computations. When the flow passes the expansion fan, consequent temperature drop leads to condensation. Then, some amount of latent heat is released from liquid droplet to vapor surroundings because the energy level in vapor phase is generally higher than liquid phase. It makes temperature drop after expansion fan more weak, and corresponding increment in kinetic energy is decreased for two-phase computations. As a result, estimated strength of expansion fan is low in two-phase computations than in single-phase computations.

This mechanism is adversely adopted for evaporation phenomena. When the flow passes shock, some amount of momentum is inverted into the thermal energy and it results in evaporation process with temperature increment. The two-phase computations show the absorption of latent heat from vapor surroundings to liquid droplets during evaporation process, which is not appearing in single-phase computations, and it leads to decreased amount in energy exchange. Therefore, estimated strength of shock in two-phase computations is

lower than in single-phase computations.

Because strength of both shock and expansion fan is low in two-phase computations, the shock-train region can be sustained for higher discharge outlet pressure, and it consequently extend the range of double-choked mode. It has important meaning when the discharge outlet pressure is close to critical back pressure, because small deviation from double-choked mode may show the huge difference in suction performance of TVC. Therefore, it can be concluded that two-phase modeling is essential component for high fidelity simulations on flow field in TVC.

Comparing between phase- changing modelings, both phase-changing models provided satisfactory results in terms of entrainment ratio, however, their local physics are slightly different to each other. The nucleation model is better choice for accurate simulation, but Hertz-Knudsen equation-based model is still remained as a reasonable choice due to its simplicity in overall computational process.

4.2 Future work

Based on accurate and efficient two-phase solver for TVC developed in this research, shape optimization study that can improve

suction performance is currently in process. It is shown that suction performance is directly related to choking condition of main nozzle, and critical back pressure is thus considered another important parameter of TVC. From this point of view, the effects of shape parameters on suction performance and critical back pressure are currently under research such as diameter of primary and suction nozzle exit, or operating pressure. Based on parametric study on shape parameters, optimum design that can enhance suction performance will be explored.

The unsteady flow physics in flow field inside TVC has been failed to gather the issue, because high fidelity of TVC due to motionless parts in operation is one of major strength. However, homogeneous nucleation phenomena in other application such as steam turbine is considered to be severe problem. Therefore, unsteady computation combined with current RANS or hybrid RANS to resolve undesirable phenomena in such application would be other challenging issue.

Furthermore, modeling on heterogeneous nucleation process can be another interesting issues for future work. In this study, only homogeneous nucleation, which occurs by surrounding environment in space, was the target for modeling the nucleation process. However,

nucleation in real physics can be occurred at the surface, and the assumption for spherical formation of droplet is thus not valid anymore. In order to describe the heterogeneous nucleation, elliptical formation of droplet should be additionally considered. The estimation modeling on such droplets is gathering the attention in academic field for various surface material, and general expression regarding this issue will have significant meaning.

References

[1] T. Sriveerakul, S. Aphornratana, and K. Chunnanond, "Performance prediction of steam ejector using computational fluid dynamics: Part 1. validation of the CFD results," *International Journal of Thermal Sciences*, vol. 46, no. 8, pp. 812–822, 2007.

[2] Y. Zhu, W. Cai, C. Wen, and Y. Li, "Numerical investigation of geometry parameters for design of high performance ejectors," *Applied Thermal Engineering*, vol. 29, pp. 898–905, 2009.

[3] N. Sharifi, R. Kouhikamali, and A. Noori, "CFD simulation of supersonic jet behavior inside thermo-compressors at different converging angles," in *(IDA) World Congress 2013, October 20-25, Tianjin, China*, 2013.

[4] Volmer, M. and Weber, A., "Keimbildung in ubersattigten gebilden," *Z. Phys. Chem*, vol. 119, pp. 277–301, 1926.

[5] J. Zeldovich, "Theory of the formation of a new phase," *J. Expl. Theoret. Physics(USSR)*, vol. 12, p. 525, 1942.

[6] J. E. McDonald, "Homogeneous nucleation of vapour condensation. i - thermodynamic aspects," *Americal Journal of Physics*, vol. 30, pp. 870–877, 1962.

[7] J. E. McDonald, "Homogeneous nucleation of vapour condensation. ii - kinetic aspects," *Americal Journal of Physics*, vol. 31, pp. 31–41, 1963.

[8] H. C. K. Yellott, J. I. and N. J. Hoboken, "The condensation of flowing steam," in *Trans. ASME*, 1937.

[9] Binnie, A. M. and Woods, M. W., "Pressure distribution in a convergent-divergent steam nozzle," in *Proc. Instrn. Mech. Engrs*, 1938.

[10] C. A. Moses and G. D. Stein, "On the Growth of Steam Droplets Formed in a Laval Nozzle Using Both Static Pressure and Light Scattering Measurements," *Journal of Fluids Engineering*, vol. 100, pp. 311–322, sep 1978.

[11] M. J. Moore, P. T. Walters, and R. I. Crane, "Davidson bj," *Predicting the fog drop size in wet steam turbines.In: Wet steam 4 conference, institute of mechanical engineer (UK)*, vol. 73, p. 37, 1973.

[12] J. G. Collier and J. R. Thome, *Convective Boiling and Condensation*. Oxford: Clarendon, 3rd ed., 1994.

[13] H. K. Cammenga, *Evaporation mechanisms of liquids*. in Current Topics in Materials Science 5, Kaldis ed., Amsterdam, North-Holland, 1980.

[14] I. W. Eames, N. J. Marr, and H. Sabir, "The evaporation coefficient of water: a review," *International Journal of Heat Transfer*, no. 12, pp. 2963–2973, 1997.

[15] D. Bedeaux and S. Kjelstrup, "Transfer coefficient for evaporation," *Physica A*, pp. 413–426, 1999.

[16] R. Marek and J. Straub, "Analysis of the evaporation coefficient and condensation coefficient of water," *International Journal of Heat Transfer*, pp. 39–53, 2001.

[17] B. Einfeldt, C. Munz, P. Roe, and B. Sjögreen, "On godunov-type methods near low densities," *Journal of Computational Physics*, vol. 92, no. 2, pp. 273 – 295, 1991.

[18] K. H. Kim, C. Kim, and O.-H. Rho, "Methods for the accurate computations of hypersonic flows: I. ausmpw+scheme," *Journal of Computational Physics*, vol. 174, no. 1, pp. 38 – 80, 2001.

[19] S. Ihm and C. Kim, "Computations of Homogeneous-Equilibrium Two-Phase Flows with Accurate and Efficient Shock-Stable Schemes," *AIAA Journal*, vol. 46, no. 12, pp. 3012–3037, 2008.

[20] "Methods for Accurate Computations of Homogeneous Multiphase Real Fluid Flows at All Speeds: Extension of RoeM and AUSMPW+ Schemes," *Computers and Fluids, in press*.

[21] S.Yoon and D. Kwak, "Three-dimensional incompressible Navier-Stokes solver using Lower-Upper Symmetric Gauss-Seidel algorithm," *AIAA Journal*, vol. 29, no. 6, pp. 874–875, 1991.

[22] J. Peter and F. Drullion, "Large stencil viscous flux linearization for the simulation of 3D compressible turbulent flows with backward-Euler schemes," *Computers and fluids*, vol. 36, pp. 1005–1027, 2007.

[23] D. C. Wilcox, *Turbulence modeling for CFD*. DCW industries, Inc., 5354 Plm Drive, La Canada, CA, 1993.

[24] F. R. Menter, "Two-Equation Eddy-Viscosity Turbulence Models for Engineering Applications," *AIAA Journal*, vol. 32, no. 8, pp. 1598–1605, 1994.

[25] F.R.Menter, "Influence of freestream value on k-omega turbulence model predictions," *AIAA Journal*, vol. 30, pp. 1657–1659, 1992.

[26] S.Sarkar, G.Erlebacher, M.Y.Hussaini, and H.O.Kreiss, "The analysis and modelling of dilatational terms in compressible turbulence," *Journal of Fluid Mechanics*, vol. 227, pp. 473–493, 1991.

[27] A. G. Gerber, "Two-Phase Eulerian/Lagrangian Model for Nucleating Steam Flow," *Journal of Fluids Engineering*, vol. 124, no. 2, p. 465, 2002.

[28] M. J. Kermani and A. G. Gerber, "A general formula for the evaluation of thermodynamic and aerodynamic losses in nucleating steam flow," *International Journal of Heat and Mass Transfer*, vol. 46, no. 17, pp. 3265–3278, 2003.

[29] J. Halama and J. Fort, "Homogeneous Nucleation of Steam in Convergent-Divergent Nozzle," *Engineering Mechanics*, vol. 21, no. 3, pp. 145–150, 2014.

[30] Y. Iga, "Numerical Investigation of Thermodynamic Effect on Unsteady Cavitation in Cascade," in *Proceedings of the 7th international symposium on cavitation*, no. 78, pp. 1–8, 2009.

[31] H. K. Dhavaleswarapu, J. Y. Murthy, and S. V. Garimella, "Numerical investigation of an evaporating meniscus in a channel," *International Journal of Heat and Mass Transfer*, vol. 55, no. 4, pp. 915–924, 2012.

[32] J. Haider, "Numerical Modelling of Evaporation and Condensation Phenomena," Master's thesis, University of Stuttgart, 2013.

[33] D. Kashchiev, "Solution of the non-steady state problem in nucleation kinetics," *Surf. Sci.*, pp. 209–220, 1969.

[34] A. Kantrowitz, "Nucleation in Very Rapid Vapor Expansions," *The Journal of Chemical Physics*, vol. 19, no. 9, p. 1097, 1951.

[35] Gyarmathy, C., Moore, M. J., and Sieverding, C. H., *Condensation in flowing steam: Two-Phase Steam Flow in Turbines and Separators*. Washington : Hemisphere Pub. Corp, 1976.

[36] A. J. White and J. B. Young, "Time-marching method for the prediction of two-dimensional unsteady flows of condensing steam," *Journal of Propulsion and Power*, pp. 579–587, 1993.

[37] P. G. Hill, "Condensation of water vapour during supersonic expansion in nozzles," *Journal of Fluid Mechanics*, vol. 25, no. 03, pp. 593–620, 1966.

[38] M. J. Berger and J. Oliger, "Adaptive mesh refinement for hyperbolic partial differential equations," *Journal of Computational Physics*, vol. 53, no. 3, pp. 484 – 512, 1984.

[39] M. J. Berger and A. Jameson, "Automatic adaptive grid refinement for the euler equations," *AIAA Journal*, vol. 23, no. 4, pp. 561–568, 1985.

[40] M. J. Berger and P. Colella, "Local adaptive mesh refinement for shock hydrodynamics," *Journal of Computational Physics*, vol. 82, pp. 64–84, 1989.

[41] J. J. Quirk and U. R. Hanebutte, "A parallel adaptive mesh refinement algorithm," *ICASE Report 93-63*, 1993.

[42] M. J. Berger and J. S. Saltzman, "Amr on the cm-2," *Applied Numerical Mathematics*, vol. 14, pp. 239–253.

[43] C. P. T. Groth, D. L. D. Zeeuw, K. G. Powell, T. I. Gombosi, and Q. F. Stout, "A parallel solution - adpative scheme for ideal magnetohydrodynamics," in *14th Computational Fluid Dynamics Conferenece*, 1999.

[44] K. H. Kim and C. Kim, "Accurate, efficient and monotonic numerical methods for multi-dimensional compressible flows part ii: Multi-dimensional limiting process," *Journal of Computational Physics*, vol. 208, no. 2, pp. 570–615, 2005.

[45] C. K. S. H. Yoon and K. H. Kim, "Multi-dimensional limiting process for three-dimensional flow physics analyses," *Journal of Computational Physics*, vol. 227, no. 12, pp. 6001–6043, 2008.

[46] H. Gerald B, Gilbert and Philip G, "Analysis and testing of two-dimensional slot nozzle ejectors with variable area mixing sections," Tech. Rep. NASA CR-2251, 1973.

[47] N. J. Georgiadis, T. Chitsomboon, and J. Zhu, "Modification of the two-equation turbulence model in NPARC to a Chien low Reynolds number k-epsilon formulation," Tech. Rep. NASA TM-106710, 1994.

[48] Y. Yang, S. Shen, T. Kong, and K. Zhang, "Numerical Investigation of Homogeneous Nucleation and Shock Effect in High-Speed Transonic Steam Flow," *Heat Transfer Engineering*, vol. 31, no. 12, pp. 1007–1014, 2010.

[49] B. J. Huang, C. B. Jiang, and F. L. Hu, "Ejector Performance Characteristics and Design Analysis of Jet Refrigeration System," *Journal of Engineering for Gas Turbines and Power*, vol. 107, pp. 792–802, jul 1985.

국문 초록

기존의 열압축기 내 수치해석 연구는 충격파가 연속적으로 발생하는 영역(shock-train region)에서 발생하는 상 변화 현상을 무시한 경우가 대다수였다. 이 경우 열압축기의 흡입 성능을 실제 실험과 유사하게 예측한 사례도 있지만 그렇지 못한 경우 또한 다수 존재하고 있다.

본 연구에서는 다상 유동 해석 및 분석을 통해 이러한 제한사항을 극복하고 개선하는 데 초점을 맞추고 있다. 상 변화 유동을 정확하게 예측하기 위해 충격파 불안정성을 배제하고 강건한 해석을 할 수 있는 AUSMPW+_N 기법, 상 변화 모델링, 적응적 격자계 세분화 기법, IAPWS-97 상태방정식 및 SBTL model 등 다양한 수치모델링들을 수치해석자에 결합하였다.

개발한 수치해석자는 연속 충격파(shock-train)가 발생하고 전단층과 상호작용 하거나 상 변화가 발생하는 등 열압축기 내 유동장에서 발생하는 물리현상과 유사한 문제들을 통해 검증하였다. 이후, 본 연구에서의 수치해석 결과의 일관성을 알아보기 위해 열압축기의 일반적인 구동 모드들을 해석하였다. 또한 연구에 사용하는 격자계가 전단층의 정확도 및 흡입성능에 미치는 영향에 대해 시험하여 해석 결과의 정확도를 뒷받침하였다. 이어서 두산중공업에서 실험한 6개의 열압축기들에 대해 단상 및 다상 유동을 적용하였는데 그 결과 다상 유동 해석이 더 정확한 결과를 도출할 수 있음을 확인하였다. 그리고 두 해석 결과의 국부 물리현상을 비교하여 다

상 유동 해석이 열압축기 내 유동장을 분석하는데 필요한 이유를 확인하고, 연구에서 사용한 2가지 상변화 모델링의 차이점을 비교하였다.

주요어 : 다상유동 수치해석, 상변화 모델, 열압축기

학 번 : 2010-30188

Name : 민 대 호